REPORT DOCUMENTATION PAGE

AFRL-SR-BL-TR-00-

0694

1. AGENCY USE ONLY *(Leave blank)*	2. REPORT DATE 01 Dec 00	3. REPORT TYPE AND DATES COVERED Final 01 April 97 – 30 September 2000

4. TITLE AND SUBTITLE

REFRACTORY ALLOY SINGLE CRYSTALS FOR HIGH TEMPERATURE APPLICATIONS

5. FUNDING NUMBERS
F49620-97-0167

6. AUTHOR(S)
Ralph H. Zee
William F. Gale

7. PERFORMING ORGANIZATION NAME(S) AND ADDRESS(ES)
Auburn University
133 South 36th St., Suite 300
Philadelphia PA 19104-3246

8. PERFORMING ORGANIZATION REPORT NUMBER

9. SPONSORING/MONITORING AGENCY NAME(S) AND ADDRESS(ES)
AFOSR/NA
801 N. Randolph St. Room 732
Arlington VA 22203

10. SPONSORING/MONITORING AGENCY REPORT NUMBER

11. SUPPLEMENTARY NOTES

12a. DISTRIBUTION AVAILABILITY STATEMENT

Approved for public release: Distribution Unlimited

12b. DISTRIBUTION CODE

13. ABSTRACT *(Maximum 200 words)*

Refractory metals and intermetallic alloys are important in high temperature aerospace systems where deformation must be maintained at a low level. This DEPSCoR project was devoted to the processing such single crystals, joining of these crystals and fracture analysis of the interface. Advances have been made in these three areas, especially in the processing of single crystals with enhanced mechanical properties. An electron beam float zone melting method was used successfully to fabricate single crystals based on three alloy systems: Ni3Al, molybdenum alloys and tungsten alloys. Due to the complex Ni3Al phase diagram, slight variations in the compositions resulted in significant difference in the growth characteristics. In the case of molybdenum alloys, the ease of single crystal formation depends on the selection of the solutes and their concentration. Little difficulty was encountered when growing the Mo-Nb alloys. The ease of crystal growth in the Ho Nb binary system was attributed to the small two-phase region and the complete solubility of Mo Nb, The growth characteristics are in accord with the interface stability criterion of a planar interface.

14. SUBJECT TERMS REFRACTORY ALLOY SINGLE CRYSTALS FOR HIGH TEMPERATURE APPLICATIONS	15. NUMBER OF PAGES 57
	16. PRICE CODE

17. SECURITY CLASSIFICATION OF REPORT	18. SECURITY CLASSIFICATION OF THIS PAGE	19. SECURITY CLASSIFICATION OF ABSTRACT	20. LIMITATION OF ABSTRACT
UNCLASSIFIED	UNCLASSIFIED	UNCLASSIFIED	UL

DTIC QUALITY INSPECTED 4

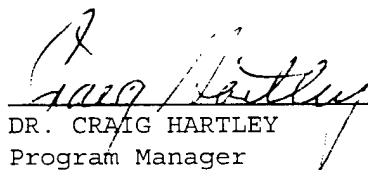NA   01 Dec 00

Acknowledgement of Receipt and Acceptance of Final Technical Report

PK

1.   Reference   F49620-97-1-0167
                    Grant or Contract Number

                    Auburn University/Zee
                    Institution and Principal Investigator

2.   Status on the FINAL REPORT covering the period
        01 Apr 97 to 30 Sep 00 is as follows

(X)   Received on 29 Nov 00

(r)   Accepted on 8 Dec 00

( )   Unacceptable - Grantee/Contractor informed of resubmission
        suspense date of _____

( )   Other: _____

DR. CRAIG HARTLEY
Program Manager

20010102 042

P. R. NUMBER: FQ8671-9900891
PROPOSAL NUMBER: 98-NA-114 (located in 8114a, pg 4)
TYPE SUBMISSION: Final Report
INST. CONTROL NUMBER: F49620-99-1-0167
INSTITUTION: Univ of Pennsylvania
P.I. NAME: Dr David Luzzi
INVENTION IND: NONE
PROJECT/TASK: 2306 AV
PROGRAM MANAGER: Dr. Hartley

****
*

1. Objective:@36.1@UNARR. ------   OBJT.

This research is to investigate the relationship between interface structure and segregation and the subsequent segregation effect on the mechanical properties of the interfaces in polysynthetically twinned (PST) titanium aluminides. The effort will focus on understanding of segregation effects on the structure and properties of gamma-gamma and alpha2-gamma interfaces (of these materials) based on the integrated experiments and computations.

2. Approach:@37.1@UNARR. ------   APPR.

The effort is a combined experimental and computational investigation of the complex interplay of segregation and interfacial structure in PST TiAl. The program consists of four major tasks: 1) growth of binary and ternary gamma-TiAl PST crystals, 2) combined high resolution electron microscopy and atomistic simulation of interfacial structure methods (including introduction of new measurement techniques, field emission TEMs and the development of interatomic potentials) to provide effective treatment of bond covalency for segregation analysis, 3) investigation of interfaces with segregation (due to ternary addition), and 4) determination of segregation effect on the mechanical properties of interfaces. The work will be collaborated with leading research organizations in the area of experimental and computational simulations.

Refractory metals and intermetallic alloys are important in high temperature aerospace systems where deformation must be maintained at a low level. This DEPSCoR project was devoted to the processing such single crystals, joining of these crystals and fracture analysis of the interface. Advances have been made in these three areas, especially in the processing of single crystals with enhanced mechanical properties. An electron beam float zone melting method was used successfully to fabricate single crystals based on three alloy systems: Ni3Al, molybdenum alloys and tungsten alloys. Due to the complex Ni3Al phase diagram, slight variations in the compositions resulted in significant difference in the growth characteristics. In the case of molybdenum alloys, the ease of single crystal formation depends on the selection of the solutes and their concentration. Little difficulty was encountered when growing the Mo-Nb alloys. The ease of crystal growth in the Mo-Nb binary system was attributed to the small two-phase region and the complete solubility of Mo-Nb. The growth characteristics are in accord with the interface stability criterion of a planar interface.

Final Report for

Refractory Alloy Single Crystals for High Temperature Applications

(AF-F49620-97-10167)

for the Period

April 1, 1997 to September 30, 2000

by

Ralph H. Zee
William F. Gale
Materials Research & Education Center

Hareesh Tippur
Mechanical Engineering
Auburn University, AL 36849

submitted to

Air Force Office of Scientific Research

Refractory Alloy Single Crystals for High Temperature Applications

Table of Content

I.   Abstract

Refractory metals and intermetallic alloys are important in high temperature aerospace systems where deformation must be maintained at a low level. This DEPSCoR project was devoted to the processing such single crystals, joining of these crystals and fracture analysis of the interface. Advances have been made in these three areas, especially in the processing of single crystals with enhanced mechanical properties. An electron beam float zone melting method was used successfully to fabricate single crystals based on three alloy systems: Ni_3Al, molybdenum alloys and tungsten alloys. Due to the complex Ni_3Al phase diagram, slight variations in the compositions resulted in significant difference in the growth characteristics. In the case of molybdenum alloys, the ease of single crystal formation depends on the selection of the solutes and their concentration. Little difficulty was encountered when growing the Mo-Nb alloys. The ease of crystal growth in the Mo-Nb binary system was attributed to the small two-phase region and the complete solubility of Mo-Nb. The growth characteristics are in accord with the interface stability criterion of a planar interface. Optimum scan rates were determined based on the compromise between the ease of single crystal formation and solute segregation. In the case of tungsten alloys, the W-Ta system with 5%Ta was selected based on compatibility criteria. Single crystals of W-Ta were successfully processed. Detailed characterization of the processed materials was conducted using x-ray Laue diffraction and electron and optical microscopy. Mechanical properties were determined as a function of temperature for all three alloy systems. The strength and ductility of Ni_3Al are superior compared to the polycrystalline state with little effect of oxidation indicative of the enhanced properties due to the absence of grain boundaries. Creep resistance in the molybdenum is enhanced by the addition of solutes in agreement with solution strengthening model based on solute size effect. Hafnium exhibits better strengthening effects in molybdenum relative to niobium due to the larger solute-solvent atomic size misfit. Results from this study confirm that the creep behavior in solution strengthened molybdenum single crystals corresponds to the Class II alloys as defined by Sherby and Burke. In addition, the creep response of these single crystals was found to be governed by the average nearest distance between the strengthening solute atoms in the lattice. In the case of W-Ta single crystals, the creep rates of the alloy single crystal were found to be three orders of magnitude lower than the pure tungsten crystals over a wide range of temperature. These results are also in agreement with the solution strengthening model.

Results with the *in-situ* NiAl – Mo bonds were generally encouraging. However, the process needs to be carefully controlled for the following reasons: i) some superheat above the eutectic temperature is desirable for wettability, but if this is excessive then melting of the bulk NiAl will occur and ii) melting will take place readily as soon as the eutectic temperature is exceeded so only a very short bonding time is required. To employ the interferometry method for fracture analysis, it was necessary to fabricate joints of particular configurations. The joining task described above was unable to provide the sample needed for this analysis. The emphasis was therefore changed to develop the technique using a standard bimaterial configuration based on copper, solder and aluminum.

II. Introduction

The performance of many aerospace components and energy/power systems can be improved with the development of such materials. The efficiency of energy systems usually increases with increasing operation temperature, which is commonly limited by the availability of suitable high temperature materials. The absence of grain boundaries in the single crystalline structure and the presence of strengthening solutes (in the case of alloys) have been found to result in significant improvements in high temperature strength and long term microstructure stability in this class of materials. These attributes are crucial for long duration operation at elevated temperatures. Many advanced energy systems require components that can sustain high temperature operation with minimal deformation over long periods of the time. For instance, fuel elements used in thermionic system for direct thermal to electric power conversion must be able to withstand a stress greater than 10 MPa at temperatures as high as 2000 K over lifetimes of over seven years [1]. Results show that these single crystals possess significantly enhanced creep resistance compared to their polycrystalline counterpart [2-3]. This is due to a combination of more stable microstructure, presence of strengthening solute atoms and the absence of grain boundaries in the single crystalline structure. The steady state creep rate of these thermionic fuel elements must be kept at a minimum by the use of appropriate high temperature structural materials. Traditional superalloys and polycrystalline refractory materials in their polycrystalline form do not possess the high temperature creep resistance and microstructural stability necessary to meet these requirements. The processing of refractory metal single crystals has been the subject of investigation at Auburn University in an attempt to develop innovative methods for fabricating such materials. This AFOSR project has concentrated on three materials with progressively higher operating temperatures: Ni_3Al, molybdenum based alloys and tungsten based alloys.

During this project, progress has been made in the processing of refractory alloy single crystals, high temperature mechanical property testing of the alloys, joining and the development of a strain gage method for measuring fracture parameters in bimaterial systems subjected to transient loading. Progress can be categorized in three main areas: (1) processing of refractory single crystals of molybdenum and tungsten, (2) joining of molybdenum single crystal to intermetallic alloys, and (3) fracture analysis. This report will be divided into these three categories.

4

III. Results and Discussion

III.1. Processing of Single Crystals

III.1.a. Basic Experimental Techniques

Electron beam zone melting is a well-known method for preparation of refractory metal rods and tubes [4-9] and was the method employed in this study. A schematic of the electron beam gun used is shown in figure 1. A pair of focussing plates were used to obtain a thin molten region. The filament was set near the lower focussing plate to provide a path for the metal vapor evaporated from the molten zone to escape thereby minimizing the out-gassing problem. The quality of the single crystals depends on the composition of the raw materials, the gas content in the initial materials, the number of scans and the final scan rate. Since the alloys developed in this study were not commercially available, all alloy rods were prepared by a powder metallurgy method. This research investigated the effects of both scan rate and scan number on single crystal formation and solute distribution. The chamber of the growth facility was evacuated by a cryopump and was maintained at a base vacuum of 10^{-6} Pa prior to heating. The maximum pressure of the chamber was 10^{-4} Pa during the growth process due to out-gassing of the rods and the wall of the hot chamber. Although the chamber wall was actively cooled by water, radiative heating from the specimen at the center of the chamber resulted in an equilibrium chamber wall temperature of about 350 K. The heat source for the specimen was an electron beam from a 20 kV DC power supply with a current capacity of 1 A. The rod was driven along its axis using a servo motor and a set of threaded rods converting the circular motion of the motor into a linear movement. The electron beam gun was held stationary. Out-gassing of the dissolved gases and evaporation of the metal vapor from the molten zone caused serious ionization problems leading to severe power output fluctuations. An emission current control system was incorporated to compensate such fluctuations.

For microstructural analysis, thin disks were cut near the end of the rods. The microstructure of the samples was analyzed using optical microscopy and scanning electron microscopy. Laue back diffraction patterns of the samples were obtained using a 30 kV - 30 mA x-ray source at a 30 mm stand-off distance. The identification of the formation of single crystals was accomplished by confirming the lack of high angle grain boundaries and Laue diffraction patterns obtained at several locations along the scan direction
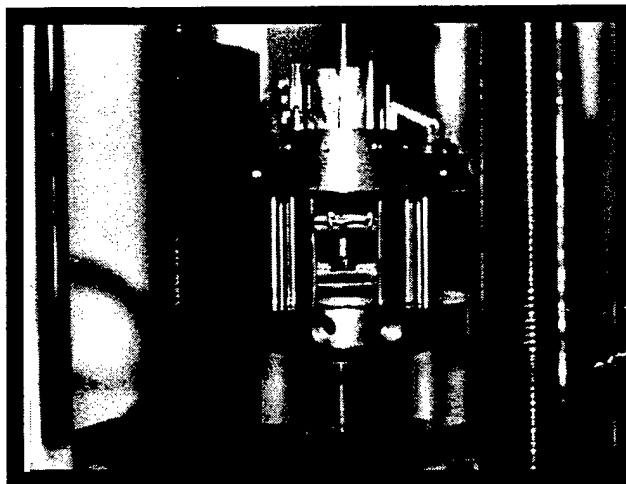
Figure 1. Photograph showing the basic structure and components of the electron gun used in the float zone method

III.1.b. Ni₃Al

Copley and Kear [10] have grown single crystals of off-stoichiometric Ni₃Al, which compositions were about 77.4 at.%Ni and 22.6at.%Al. The melt was poured into a preheated alumina mold and solidified from one end by gradient cooling. Most Ni₃Al single crystal were grown using modified Bridgman techniques [11-14] and the horizontal zone melting method [15] in an argon atmosphere or vacuum. The alloys with compositions below the eutectic composition of 24.2 at.%Al can be processed into the single crystalline structure easier compared to the stoichiometric alloy. This is because cored structures are formed 'with gamma (γ) dendrites which transform upon further cooling to a γ+γ' mixture. Stoichiometric or Al-rich Ni₃Al solidify dendritically with the formation β-NiAl occurring first. The precipitate β-NiAl suppresses the grain growth of γ' (Ni₃Al) perpendicular to the growth direction, resulting in the columnar structure of Ni₃Al [16]. This complex microstructure evolution may be responsible for the difficulty in growing single crystals of stoichiometric Ni₃Al.

The objective of this research was to investigate the effects of two parameters, superheat and growth rate, on crystal growth processing of binary Ni₃Al alloys. Results will contribute to selecting the optimized processing parameters for growing Ni₃Al single crystal, and generate single crystalline intermetallics for joining study.

Three compositions of Ni₃Al (with 23.5 atomic % Al, 24.0 atomic % Al and 25.0 atomic % Al) were examined. An 8-mm alumina tube with a conical tip was used to initiate the growth process. These three compositions were selected due to their relative positions in the phase

diagram. The Ni-Al system in the vicinity of Ni$_3$Al consists of a eutectic reaction at 24.2% Al and a peritectic reaction with a peritectic composition at about 25% Al. Therefore the growth characteristics may be considerably different with small variations in composition. The crystal growth characteristics of the three alloys were investigated in terms of solidification rate and superheat temperature

The first several attempts were also made to grow Ni$_3$Al crystals using pure nickel single crystal seed and Ni$_3$Al bicrystal seed without the use of any crucible. The Ni$_3$Al specimen rods were directly heated by electron bombardment. The temperature reading from molten zone (measured directly using the two-color pyrometer) was between 1750 K and 1770 K. The scan speeds were varied between 15mm/hr and 30mm/hr. No single crystal was obtained using this direct heating technique. A unidirectional solidified microstructure similar to that observed by Hirano [16] was found. This indicates that the unstable and small size of the molten zone generated by the direct bombardment of the focused electron beam prevents the formation of single crystalline.

Following the first set of failure, a decision was made to growth the crystals in a crucible made of alumina. The alumina tube was enclosed in a molybdenum tube which served as the susceptor for the electron beam gun. The thickness of the molybdenum susceptor is 1.5mm and thermal distribution. To study the effect of superheating, a constant withdraw speed of 15mm/hr was used. It was found that the optimum superheat for crystal growth depends on composition. A second series of experiments were conducted to study the effect of growth rate under the optimum superheat condition. In these experiments, scan rates of 5mm/hr to 75mm/hr were used.

The quality of crystal is defined as reciprocal of grain density. A single crystal would therefore have the highest quality. In this series of experiments, a constant withdraw speed of 15mm/hr was used for different melt temperatures. The objective of this study is to determine the optimum superheat and its dependence on composition. Table 1 summarizes the results of this set of experiments. Ni$_3$Al binary alloy crystals with three compositions examined have different microstructure morphologies. Ni$_3$Al with 23.5% Al possesses large amount of dendrites comparing with the other two compositions. Stoichiometric Ni$_3$Al (25%Al) has the fewest amounts of dendrites and also has different types of dendritic morphology. These morphologies are related to the shape of the phase diagram. Ni$_3$Al with 23.5% Al has the largest temperature difference between the liquidus line and three-phase reaction temperature compared to that for the alloy with 24% Al and 25%Al. This implies that the 23.5% Al alloy possesses the widest mushy zone. This feature enhances dendritic growth resulting in the observed structure. Such morphology at liquid/solid interface is not favorable for producing a single crystalline structure. However a high degree of superheat will lead to a large temperature gradient at liquid/solid interface resulting a reduction in the mushy zone. This implies that the optimum

superheat for single crystal growth in the alloy with 23.5% Al should occur at the largest superheat amongst the three compositions studied. This is in agreement with the experimental findings given in Table 1.

Table 1: Summary of Results for Optimum Superheat

Comp (%Al)	Melting Point (K)	Superheat Temp Range (K)	Optimum* Superheat Temp Range (K)
23.5	1663	31 – 363	200 – 300
24.0	1658	22 – 311	35 – 115
25.0	1683	7 – 406	40 – 140

*Optimum Superheat Range Temperature is defined as the range of superheat that results in a >50% probability of producing single crystal using a scan rate of 15mm/hr.

Using the optimum superheat obtained in the above section as a guideline, a series of experiments were conducted to determine the optimum growth rates for the three compositions. Table 2 shows the results of this set of experiments. The step size used in the experiments is 5mm/hr. Results show that the optimum growth rate is relatively independent of alloy composition and is between 15 and 30 mm/hr. These results are in good agreement with two studies by Hirano and his colleagues [16]. They determined that best cooling rates for unidirectional solidification of stoichiometric Ni_3Al were 13mm/hr and 25mm/hr.

Table 2: The Optimized Growth Rate for Ni_3Al Crystals

Comp (%Al)	Growth Rate Range (mm/hr)	Range of Superheat (K)	Optimized Growth Rate Range (mm/hr)
23.5	10 – 45	220 - 250	15 – 35
24.0	5 – 35	140 - 150	15 – 25
25.0	15 – 75	80 - 100	15 – 40

Different compositions produce different microstructures. Difference in the cooling temperature history will also produce different microstructures for the same alloy composition. The Ni_3Al binary alloys, 23.5 at%Al, 24 at.%Al, and 25 at.%Al, show quite different microstructures, which are shown in figures 2 to 4. In those figures as well as in other microstructure photographs, R represents crystal growth rate, G represents temperature gradient at liquid/solid interface. The eutectic microstructure of Ni_3Al (24 at.%Al) is shown in figure 5.

From the microstructures, Ni_3Al with 23.5 at.%Al has a thicker dendrite skeleton than the Ni_3Al with 24 at.%Al, while Ni_3Al with 25 at.%Al, which is a stoichiometric compound, has a different dendrite morphology from the other two alloys. According to the Ni-Al phase diagram, the initial γ phase will precipitate first from the melt when the temperature meets the liquidus for hypoeutectic alloys with 23.5 at.%Al and 24 at.%Al. The alloy with 23.5 at.%Al is little further away from the eutectic point than the 24 at.%Al, and so has a thicker dendrite skeleton.

The 25 at.%Al Ni_3Al alloy can be readily distinguished from the other two alloys, as γ phase precipitates from the melt first when solidification begins, producing a different dendrite morphology. Although these three alloys are all in the γ' phase region below 1000 °C, dendrites will not disappear under non-equilibrium conditions because solid diffusion takes place too slowly. Annealing heat treatment may remove the dendrite γ and produce single phase γ' (Ni_3Al), but it is difficult to resolve the γ phase due to its large difference from the γ' phase composition and crystal structure, which β has B2 structure and γ' has $L1_2$ structure.

The microstructure of Ni_3Al (25 at.%Al) from electron beam zone melting without a crucible is shown in figure 6. The temperature of the molten zone was measured to be 1480 °C by a pyrometer. At the steady crystal growth stage, γ' precipitates from the liquid, which is a product of a peritectic reaction. If the growth rate was increased suddenly or instabilities arose in the molten zone, a band of β phase was formed which is shown in the microstructure. However, the β phase always existed during crystal growth. Figure 6 also shows that the crystal started to grow from a bicrystalline seed. At the beginning it retained its bicrystal form, but after a short period of growth, extra grain boundaries appeared. It shows that multigrains appeared even when the solidification originated from a bicrystalline seed. The aluminum concentration redistribution along the growth direction was measured using SEM/EDS and a typical result is shown in figure 7. The profile indicates that the solidification remained in a steady state during processing, and the initial transient stage and final transient stage were short compared with the steady stage.

In summary, optimized crystal growth parameters for Ni_3Al with three different compositions, 23.5 at.%Al, 24 at.%Al, and 25 at.%Al, were obtained under the specific solidification conditions. The optimized superheat ranges for these three different alloys are 200 to 300 °C, 35 to 115 °C, and 40 to 140 °C, respectively. The optimized growth rates for these three alloys are 15 to 35 mm/hr, 15 to 25 mm/hr, and 15 to 40 mm/hr, respectively.
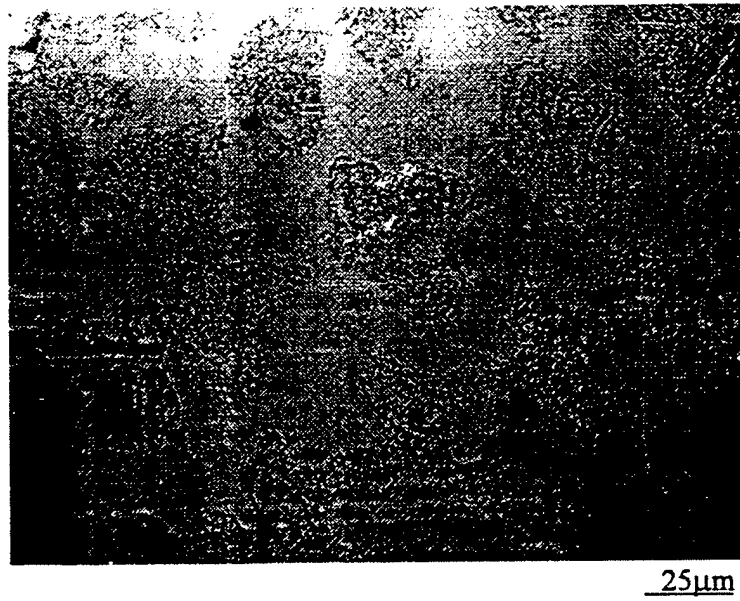
9

25μm

Figure 2. Ni$_3$Al (23.5 at.%Al) microstructure.
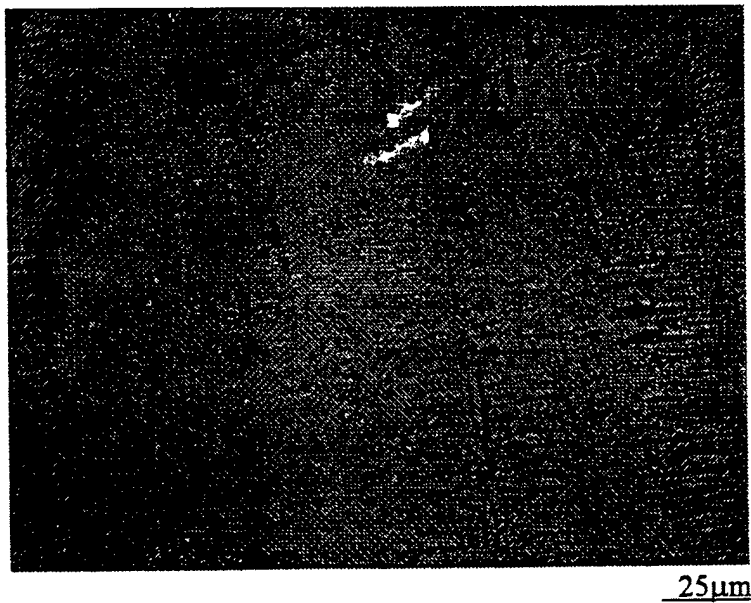

25μm

Figure 3. Ni$_3$Al (24 at.%Al) microstructure.

10

Figure 4. Ni₃Al (25 at.%Al) stoichiometric microstructure.

Figure 5. Ni₃Al (24 at.%Al) eutectic microstructure.
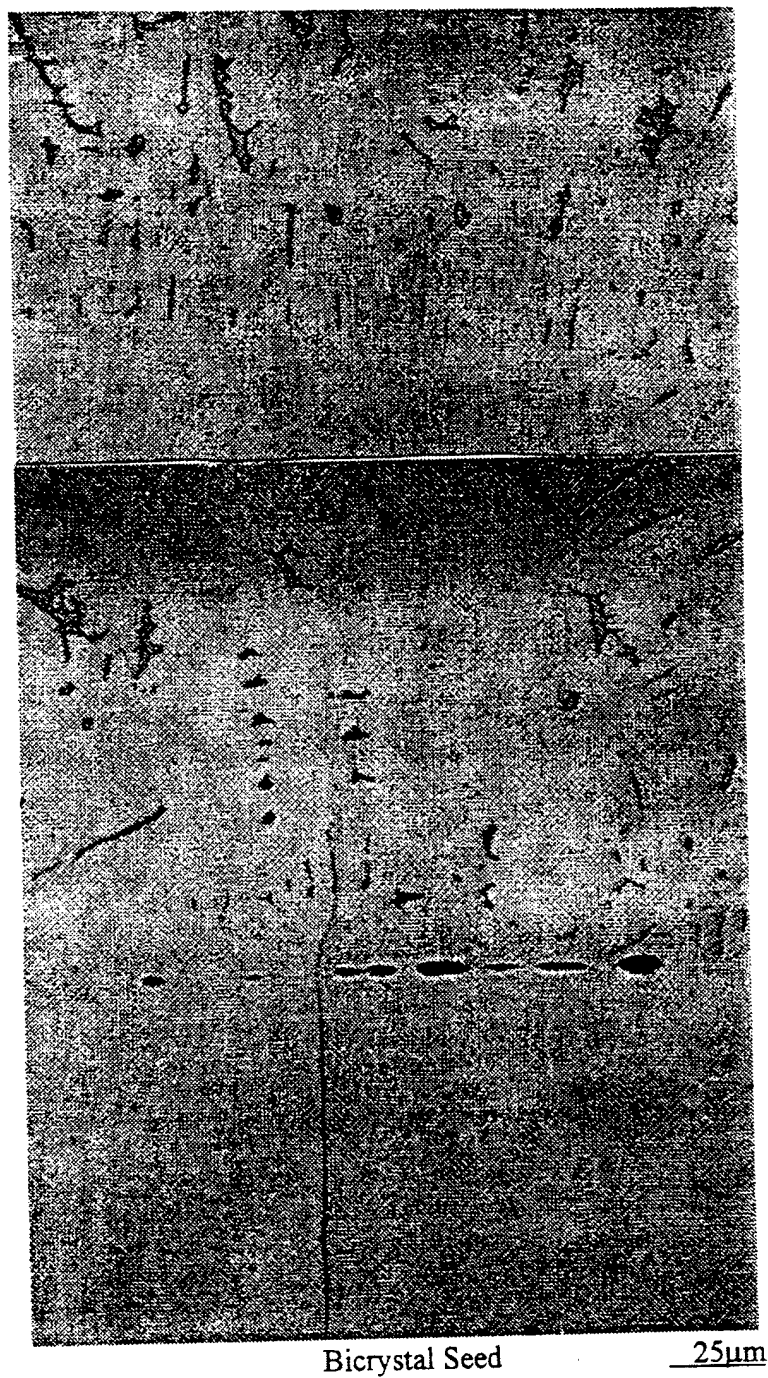
Bicrystal Seed   25µm

Figure 6. Microstructure (etched) of Ni₃Al (25 at.%Al) which originated from a bicrystalline seed using direct electron beam zone melting.
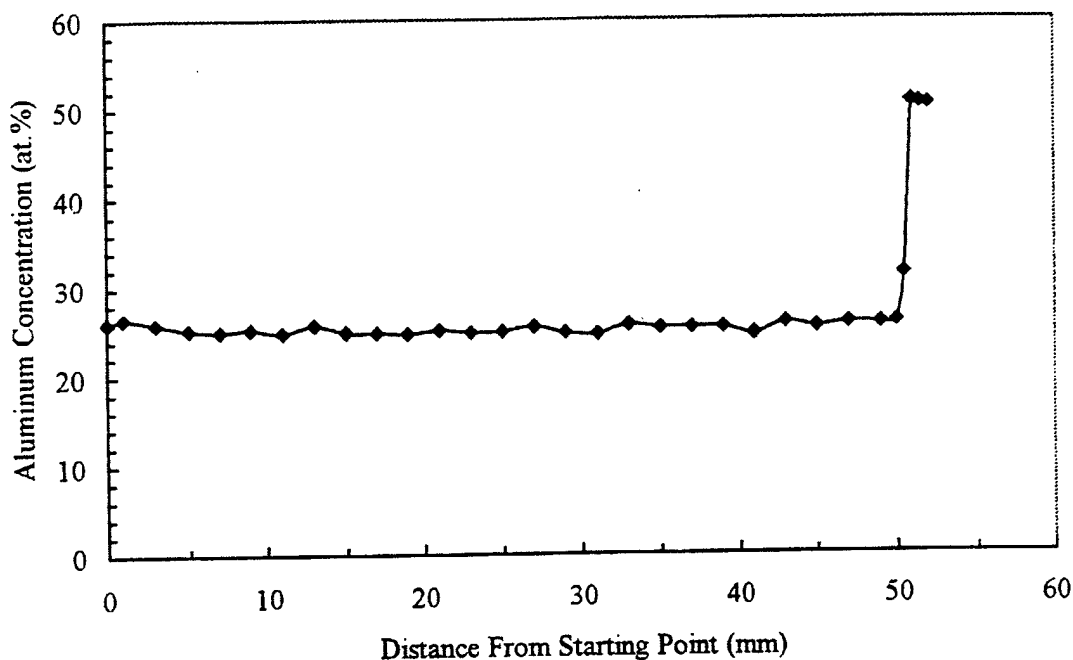
Figure 7. A profile of aluminum concentration along crystal growth direction (25 at.%Al alloy, R = 15 mm/hr, G = 20 °C/mm, melt temperature = 1527 °C).

III.1.c. Molybdenum Based Alloys

A detailed study of the growth characteristics of molybdenum-based single crystals using the electron beam float zone technique was completed. Single crystalline alloys of Mo-Nb, Mo-Hf, and Mo-Hf-C were successfully fabricated and an analysis for the two binary systems was conducted. The compositions of the alloys investigated in detail are given in Table 3. Scan rates of 11, 22 and 55 mm/h were used to determine the effect of growth rate (and its dependence on alloy composition) on single crystal growth characteristics. These three scan rates correspond to the optimum range that the facility is capable of providing. Results show that it is significantly easier to form single crystals from the Mo-Nb system compared to the Mo-Hf system. For example, single crystals of molybdenum alloys with up to 11% Nb can be formed even at a high scan rate of 55 mm/hour whereas a very low rate of 11 mm/h is required to form single crystals of Mo with only 2% Hf. In addition, the maximum scan rate for single crystal formation depends on the alloy composition in a reverse manner; high alloying contents lead to slower scan rates. The critical scan rates for Mo-1%Hf, Mo-2.75%Hf and Mo-3.71%Hf-1%C were found to be 55 mm/hour, 22 mm/hour and 11 mm/hour respectively. Solute segregation was present along the scan direction due to the zone refining effect. Reduction of this solute segregation can be achieved by either using high scan rates or stirring the molten zone by rotating the two

13

segments of the rod (above and below the molten zone) in opposite directions [17]. Since the latter method was more difficult to achieve in a high voltage environment, the fast scan rate approach was chosen. In addition, out-gassing of the samples was a serious problem due to the 5% porosity in the raw materials. The zone scan speed had to be kept sufficiently low to facilitate proper degassing of the samples during melting and to maintain a stable liquid-solid interface. Multiple zone passes were needed to further minimize the out-gassing problem in order to obtain the single crystalline structure. However, the amount of material loss due to liquid phase evaporation is affected by the number of scans and the scan speed. Therefore, optimum procedures for specific alloy compositions had to be determined experimentally.

An analysis developed by Biloni [18,19], based on the requirement of maintaining a planer interface during zone scanning, was conducted on the results obtained. Applying this model with parameters corresponding to the experimental conditions used, we arrived at the following inequity to describe the maximum scan rate possible for the growth of single crystals:

$$(\Gamma_s K_s + \Gamma_l K_l) / (K_s + K_l) > -m_l C_o (1/\xi_o + 1)(V/D_l) \exp(-V\chi_d d_s/D_l d_l) \qquad (1)$$

where Γ_s and Γ_l are temperature gradients in the solid and liquid phases, K_s and K_l are thermal conductivities in the solid and liquid phases, m_l is the slope of the liquidus line, C_o is the solute concentration, ξ_o is the equilibrium partition coefficient, V is the growth rate (scan rate), D_l is the diffusion constant of the solute in the molten zone, χ_d is the size of the diffusion boundary layer ahead of the interface d_s and d_l are the densities of the solid and the liquid phases. When considering the molybdenum-based systems (Mo-Nb and Mo-Hf), it is reasonable to assume that all the parameters are the same except m_l, C_o and ξ_o. The experimental parameter of interest here is the term V, the maximum scan rate for single crystal production (or to maintain a planer interface). Figure 8 shows a comparison of the calculated maximum scan rate as a function of Hf content with experimental data. According to this analysis, there is a good general agreement between the model prediction with observation. The model slightly overestimates the maximum scan rate condition, which is likely due to the disturbance of the growth process as a results of out-gassing of the materials which the model does not account for. The difference between Mo-Nb and Mo-Hf is in the terms m_l and ξ_o. Both m_l (the liquidus slope) and ξ_o (the equilibrium partition coefficient) depend on the shape of the phase diagram. The values of m_l for Nb and Hf in Mo are -1.3 and -4.5 K/%solute, respectively. The ξ_o values for Mo-Nb is approximately 0.43 whereas that for Mo-Hf is about 0.16. Based on these parameters, the maximum scan rate for growing Mo-Nb single crystals is approximately seven times that for Mo-Hf. This is shown in figure 9 which clearly indicates that even at a high scan rate of 55 mm/h, the condition is appropriate for the formation of single crystals for molybdenum even with 11% Nb.

Table 3. Composition of the Molybdenum-Based Alloys Investigated

Nominal Composition (Atomic Percent)
Mo-2%Nb
Mo-11%Nb
Mo-11%Nb-0.18%Hf-0.43%C
Mo-018%Hf-0.43%C
Mo-0.8%Hf-0.43%C
Mo-1%Hf
Mo-2%Hf
Mo-2.5%Hf
Mo-2.5%Hf-10%Nb
Mo-2.75%Hf
Mo-3.7%Hf-1%C
Mo-10%Hf-2%C
Mo-15%Hf

Figure 8. Comparison of experimental data with prediction for the Mo-Hf system. The dash line represents the prediction for the maximum scan rate for single crystal formation. The solid line represents the maximum scan rate determined experimentally.
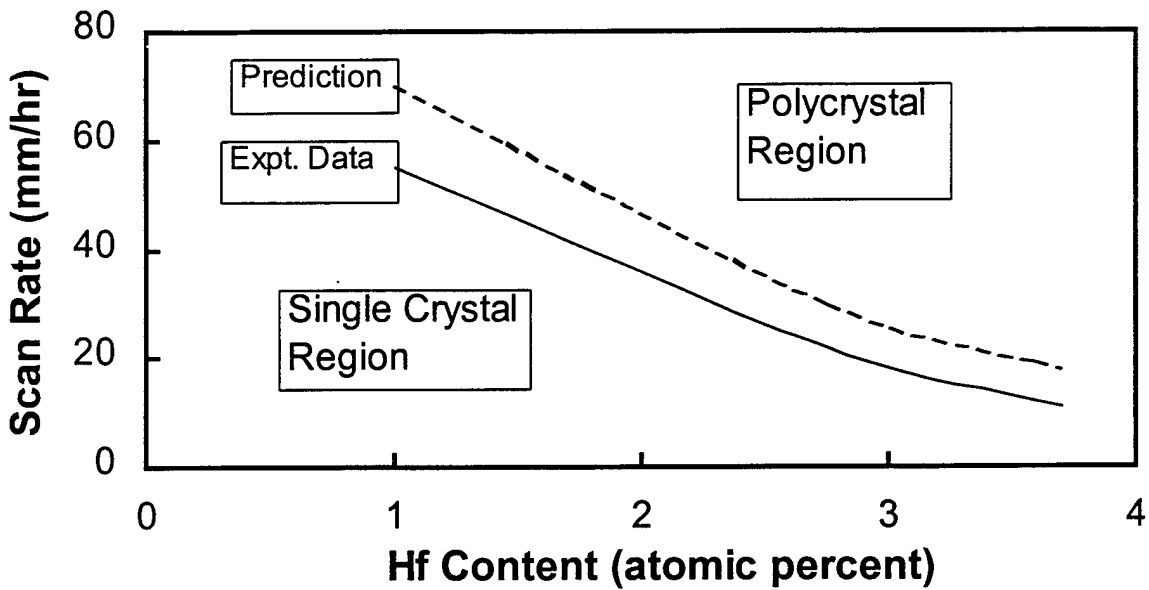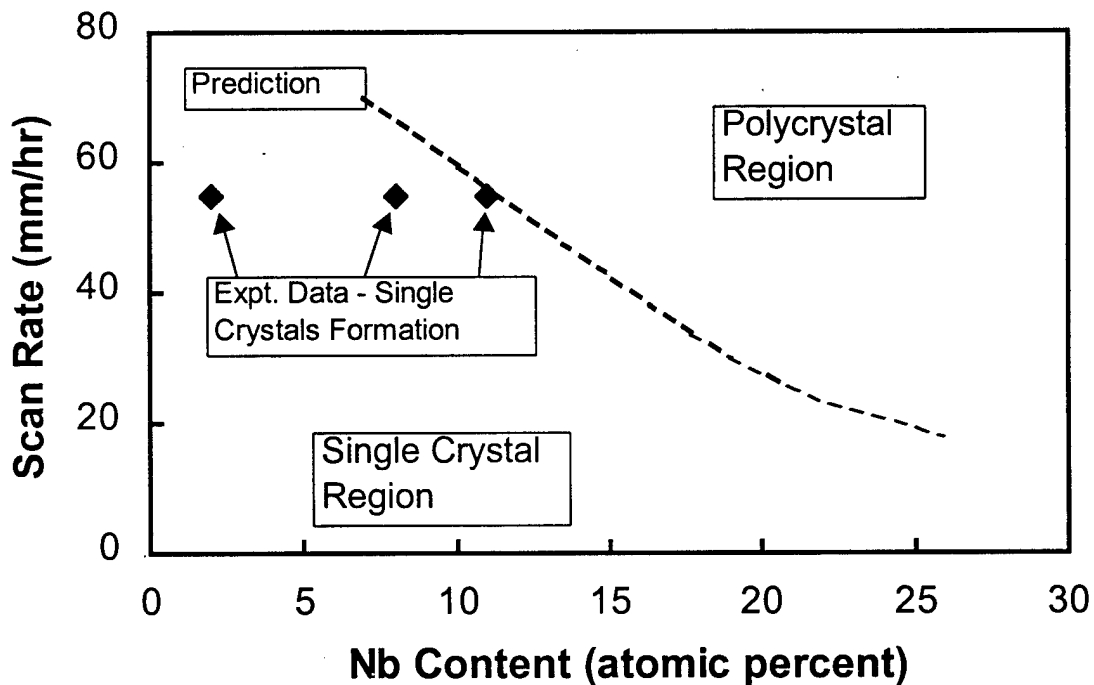

Figure 9. Comparison of experimental data with prediction for the Mo-Nb system. The dash line represents the prediction for the maximum scan rate for single crystal formation. The diamond data points represent the three single crystals processed successfully for the Mo-Nb system and they fall within the predicted range.

The surface morphology of the processed crystals depends on the quality of the growth. Normally a smooth surface was obtained when the growth condition is appropriate for single crystal formation whereas a "layer"-like surface structure is associated with a polycrystalline structure. This is illustrated in figures 10 and 11. Figure 10 corresponds to Mo-2%Hf scanned at a low rate of 11 mm/h forming a single crystalline structure whereas figure 11 was taken from the same alloy but processed at a higher rate of 55 mm/h resulting in a polycrystalline structure. The single crystalline structure exhibits a much smooth surface morphology compared to its polycrystalline counterpart.

Chemical analysis based on the energy dispersive technique was conducted on all the specimens processed. No composition segregation (or variation) was found in the radial direction in any of the as-grown crystals. However, composition variations were observed along the scan direction. The composition profile (for Hf) of a Mo-3.71%Hf-1%C single crystal as a function of axial position is given in figure 12 showing a slight increase in Hf content with growth as expected. The degree of zone refining is relatively small and does not lead to a significant change in the overall composition in the Mo-Hf system. No segregation effect was observed in the Mo-Nb system. This is due to the difference in the phase diagram between Mo-Nb and Mo-Hf in that the two phase region in the Mo-Nb system is smaller.

In summary, three types of alloys, Mo-Nb and Mo-Hf and Mo-Hf-C, were successfully grown into single crystals using an electron beam zone melting method. The growth characteristics were found to depend on the size of the two phase region of the material systems selected. Experimental results show that it is easier to grow single crystals of Mo-Nb compared to Mo-Hf and Mo-Hf-C due to the smaller temperature difference between the solidus and the liquidus lines in the former and complete solid solubility between Mo and Nb. For molybdenum alloys with up to 11% Nb, a high scan rate of 55 mm/hour was found to be capable of producing satisfactory crystals. For Mo-Hf, the optimum scan rate depends on the Hf content in an inverse manner: higher Hf contents require slower scan rates. The maximum Hf content in Mo-Hf alloys was limited to about 5% beyond which single crystals could not be formed regardless of the scan rate employed. Segregation of hafnium was observed along the growth direction and factors controlling such an effect were examined. Experimental results based on a compromise between solute segregation and ease of crystal formation suggest that the optimum scan rate for Mo-Hf to be 22 mm/hour.
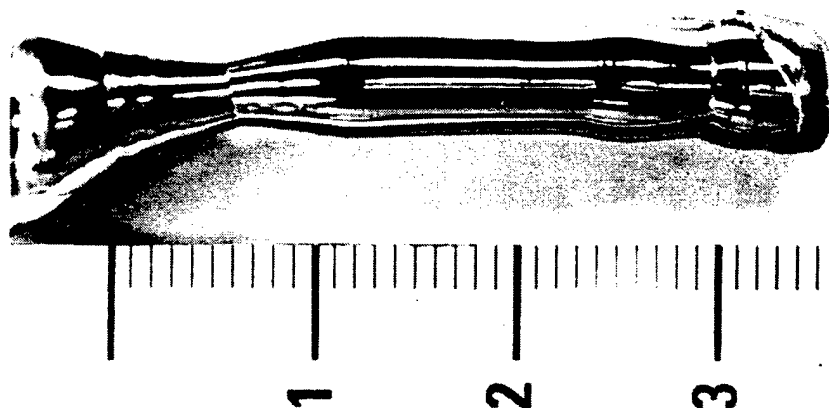
Figure 10. Surface morphology (smooth) of a Mo-2%Hf single crystal grown at a rate of 11mm/h.

Figure 11. Same as figure 10 but for a polycrystal grown at a rate of 55mm/h. Notice the rougher surface morphology compared to the single crystal.
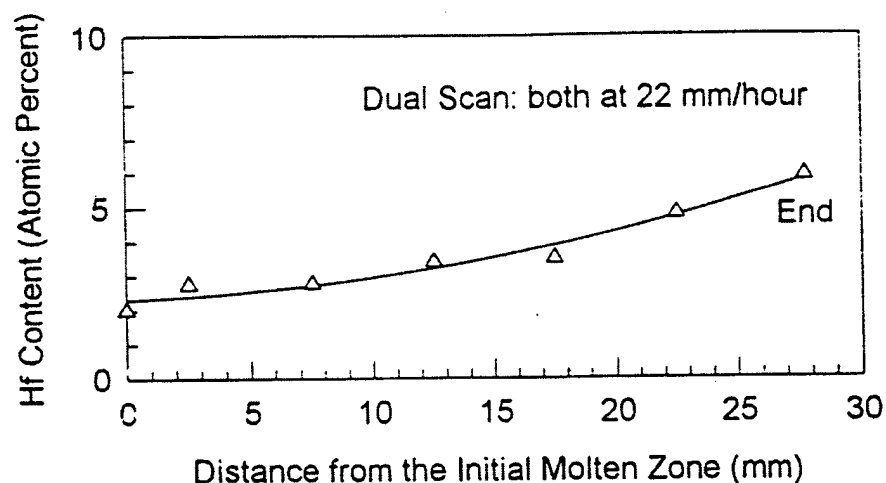
Figure 12. Concentration profile for Hf showing slight segregation due to zone refining.

III.1.d. Tungsten Based Alloys

The feasibility of processing tungsten alloy single crystals was examined. The first task at hand is to determine the appropriate strengthening agent for tungsten. Tungsten with 5% tantalum was selected based on the following justifications. The growth characteristics and the creep properties of alloys depend on the following parameters with the preference indicated: (1) Crystal structures of the solute elements (similar structure is preferred), (2) Difference in the melting temperature between solute and solvent (small temperature differential is preferred), (3) Elastic modulus (larger modulus is preferred), (4) Atomic mobility (low mobility is preferred), (5) Electron-atom ratio (high is preferred), (6) Atomic size difference (larger difference is preferred), and (7) Vapor pressure (similar to W is preferred).

Based on criterion 1, we have identified five possible solutes: Mo, Cr, Ta, V and Nb (or Cb). All these elements are of the body-centered cubic structure (same as W). Although Re and Hf are frequently used as modifier for W (Re for ease of low temperature processing and Hf as a carbide former), we have excluded them for crystal growth due to the difference in their crystal structure with W (Re is hcp and Hf is bcc at high temperature and hcp at low). The phase diagrams for the two systems clearly indicate the complex phases that occur as a result of the dissimilar crystal structures. Table 4 shows the melting temperature of the elements of interest, including tungsten for reference. In terms of this parameter, Ta is most suitable and Cr is the least.

Solutes with high elastic moduli and low atomic mobilities are in general effective in improving the temperature creep resistance. In the case of refractory alloys, the trend of the elastic modulus is:

$$W > Mo > Cr > Ta > V > Nb \tag{2}$$

19

Table 4. Melting Temperature of Elements of Interest.

Element	Melting Temperature ($^{\circ}C$)
W	3410
Ta	2996
Mo	2617
Nb	2468
V	1890
Cr	1857

The diffusivity (D) versus T/T_M (T_M is melting point of metal in Kelvin) for those metals changes in the following order [20, 21],

$$Ta = V > Nb = Mo > Cr > W \qquad (3)$$

If T_M is not considered as a factor (in terms of temperature only), the diffusivity of Ta is smaller than that of Nb. Diffusivity is a function of temperature through the equation: $D = D_o \exp(-Q_{S-D}/RT)$. The values of activation energy, $Q_{self-diffusion}$, for Ta and Nb are 98.7 and 96.0 kcal/mole respectively. The D_o for Ta and Nb are 0.12 and 1.1, respectively [21]. Consequently, at the high temperature of interest (above $1800^{\circ}C$), the diffusivity of Nb is at least ten times greater than that of Ta, making Ta a good candidate for high temperature applications.

The rate of strengthening of niobium, tantalum, molybdenum, and tungsten by substitutional solutes is related primarily to the increase in electron-atom ratio. The valence electronic structure of Ta is $5d^3 6s^2$ and that of Nb is $4d^4 5s^1$. The other solute elements have similar electronic structures and therefore the role of electron to atom ratio is not important in this consideration.

Size effect also plays a role in solid solution strengthening. The direct interaction between solute atoms and dislocations is one of the factors which contribute to solid solution hardening. The presence of a solute atom, different in size from that of the matrix, results in a localized strain field. This strain field interacts with the strain field of the dislocations resulting in restricted motion of the dislocations. The misfit parameter δ is defined as

$$\delta = 1/a \, (\partial a/\partial c) \qquad (4)$$

where a is the lattice constant of the material. This misfit parameter is mathematically equivalent to the linear size-factor, lsf:

$$lsf = 1/r_{oA}(\partial r_o/\partial c) \qquad (5)$$

where r_{oA} is the Seitz radius and $r_o = (3\Omega/4\pi)^{\frac{1}{2}}$. Table 5 gives the volume size-factor (Ωsf), linear size-factor and limiting concentration (c_{max}) obtained experimentally for some tungsten alloys [22]. In this case, the larger the size difference, the more effective is the solute in providing strengthening. Although the W-Cr has the highest misfit factor, Cr is not acceptable due to other reasons. The W-Ta system is the next best system.

For ease of single crystal processing without significant loss of solute, it is important to have the vapor pressure of the solute to be similar to that of tungsten at the melting point. The vapor pressure of Nb is thirteen times higher than that of Ta in high temperature range [23]. The vapor pressures of the solutes of interest at 3410°C (melting point of W) are given in Table 6. Tantalum is the obvious choice.

Table 5. Size Parameters for the Alloys of Interest.

System	c_{max} (at.%)	Ωsf (%)	lsf(%)
W-Cr	20	-21.73	-7.84
W-Mo	25	-1.55	-0.52
W-Nb	25	+7.33	+2.39
W-Os	7.5	-7.82	-2.68
W-Pt	4.0	-2.71	-0.91
W-Ru	12	-5.35	-1.82
W-Si	20	+0.81	+0.27
W-Ta	*45*	*+11.01*	*+3.54*
W-U	2.0	-0.82	-0.74
W-V	30	-10.60	-3.66

Table 6. Vapor Pressure of Solutes and Tungsten at 3410°C.

Element	Vapor Pressure (torr, mmHg)
W	0.01
Ta	0.05
Mo	2.5
Nb	2.5
V	700
Cr	Beyond boiling point, above 1 atmosphere

As a result of the considerations discussed above, we have selected W-Ta to be the system for further investigation. A concentration of 5 atomic % Ta will be used. This solute level (up to 5%) is considered to be an optimum composition to retain the basic properties of tungsten and fully utilizing the strengthening effect of the solute.

Having identified the W-5%Ta being the candidate material, a feasibility study was conducted to determine the processing parameters to fabricate this alloy into the single crystalline form. The electron beam zone melting method was used and single crystals of W-5%Ta were successfully processed using a growth rate of 11 mm/h. Scan rates faster than this resulted in the retention of the polycrystalline structure. Figure 13 shows a photograph of a long W-Ta single crystal (approximately 100mm long) processed in this project. Figures 14 and 15 show the back-reflection Laue patterns obtained from two of these single crystals in two different orientations (using the seeding technique): [001] and [111]. The composition of the grown W-Ta crystals is also very uniform with little sign of zone refining. This is illustrated in figure 16 which shows little variations in the composition (determined by EDS analysis) as a function of growth direction. The deviation of Ta content (7 atomic percent) from the original composition of 5 atomic percent is most likely due to the calibration problem of the semi-quantitative analysis of the microscope.
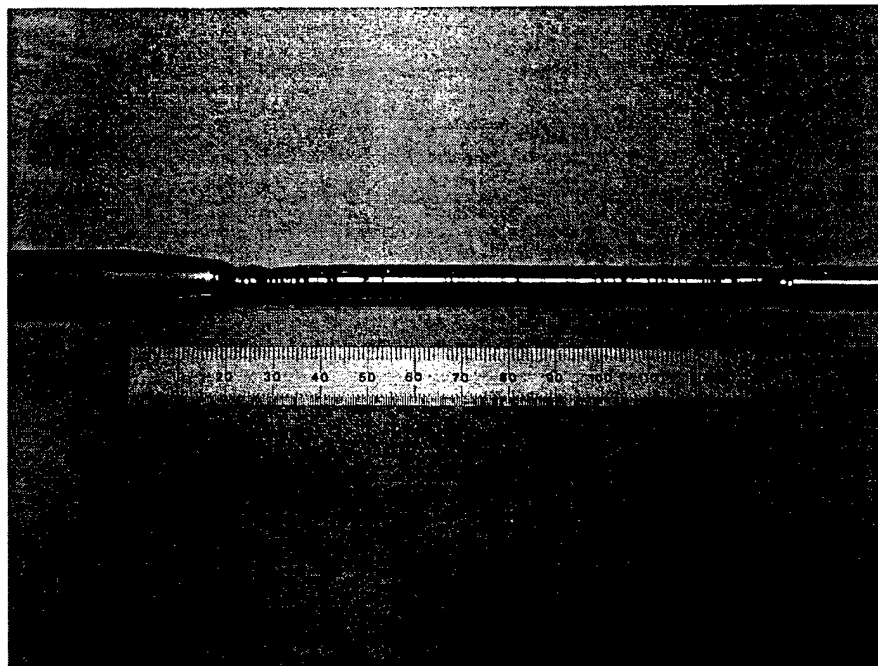
Figure 13. Photograph showing a W-Ta single crystal.

Figure 14. Back-reflection Laue for the W-Ta alloy in the [001] orientation.
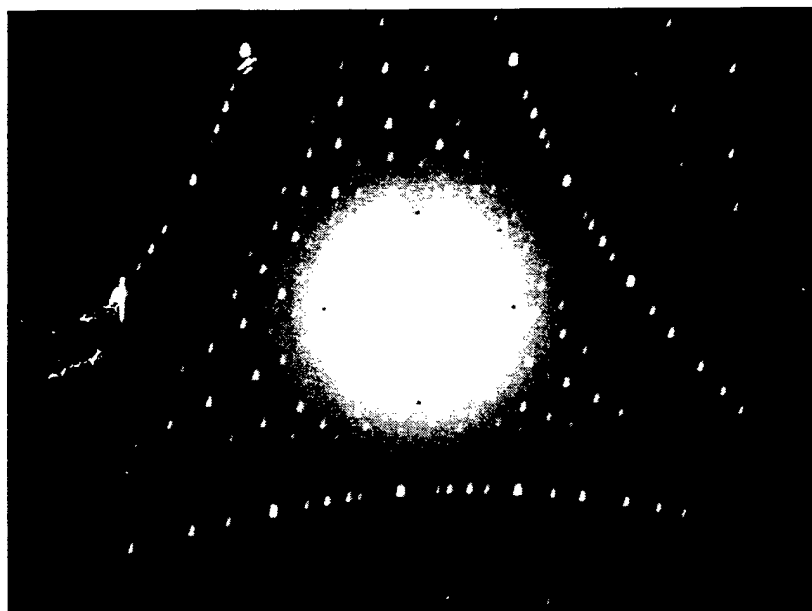
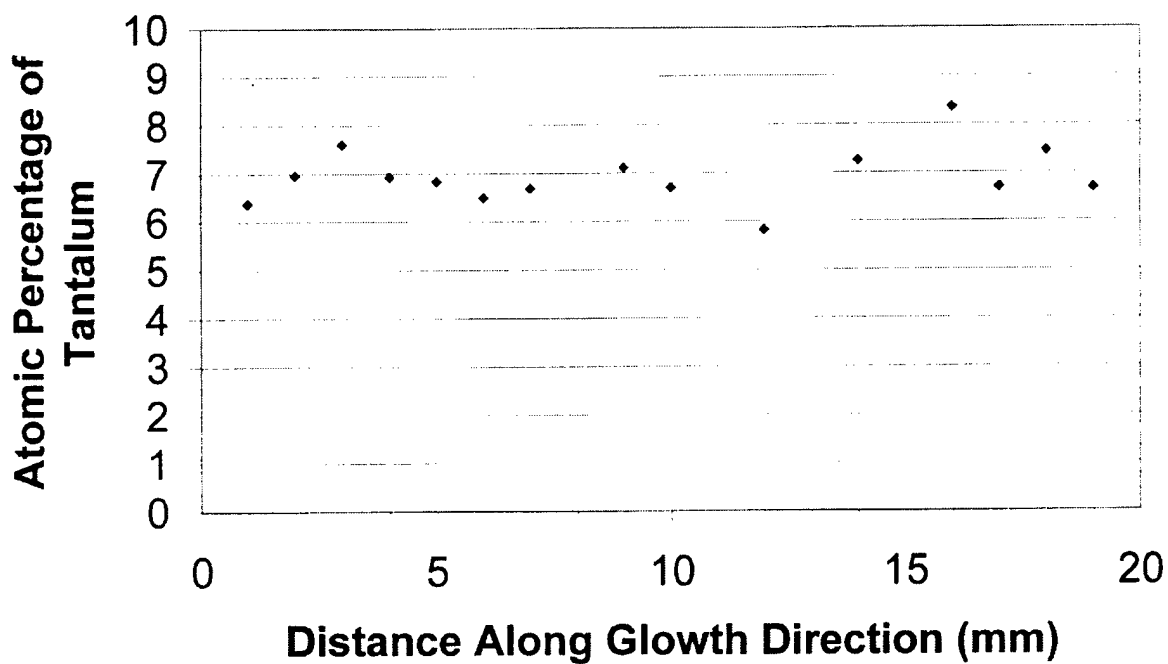Figure 15. Back-reflection Laue for the W-Ta alloy in the [111] orientation.

Figure 16. Composition profile of Ta as a function of growth direction determined for a
W-Ta single crystal showing little segregation.

III.2. Mechanical Properties

III.2.a. Ni₃Al

Mechanical properties (stress strain relationship) were determined for the Ni_3Al single crystals under two conditions: non-oxidized and pre-oxidized states. The purpose is to identify the role of grain boundaries in this material. It is generally agreed that the lack of strength of ductility in this material is due to weak grain boundaries. With the success in the processing of single crystalline Ni_3Al, it is possible to determine this effect by conducting tensile test of crystals under these two conditions. The single crystalline Ni_3Al materials were subjected to tensile tests at room temperature and at elevated temperatures (from 500 °C to 900 °C) under a protective argon environment. The specimens were preoxidized at 500 °C, 600 °C, 700 °C, 800 °C, and 900 °C for 24 hrs, which were the same temperatures as those used for the non-oxidized specimens. The tensile tests for the preoxidized specimens were also carried out at the same temperature. Ideally, a constant crystal orientation would have been used. However, the orientation of the Ni_3Al crystals could not, in practice, be controlled. Figures 17 to 19 show the relationships for yield stress, ultimate stress and elongation of Ni_3Al single crystals with temperature, respectively. It is evident from these figures that the state of oxidation has essentially no effect on the mechanical property of this material. This is indicative that the single crystalline Ni_3Al is not susceptible to oxidation confirming that the grain boundaries in polycrystalline Ni_3Al are the source of weakness in this material. Furthermore the strength and the ductility of the single crystals are high compared to their polycrystalline counterpart in agreement with weak grain boundaries. The fracture surface morphologies at different temperatures were analyzed. All samples show transgranular fracture (both unoxidized and pre-oxidized states) in agreement with the mechanical property data.

In summary, preoxidized Ni_3Al single crystalline materials possess anomalous yield stress behavior. The yield stress peak temperature is about 700 °C. Preoxidized and non-oxidized Ni_3Al single crystalline materials do not have an obvious discrepancy in strength and ductility. However, the strength of the non-oxidized Ni_3Al single crystalline materials is slightly better than that of the preoxidized ones, especially away from the yield stress peak temperature. The ductility of nonoxidized samples is slightly lower than that of preoxidized ones.
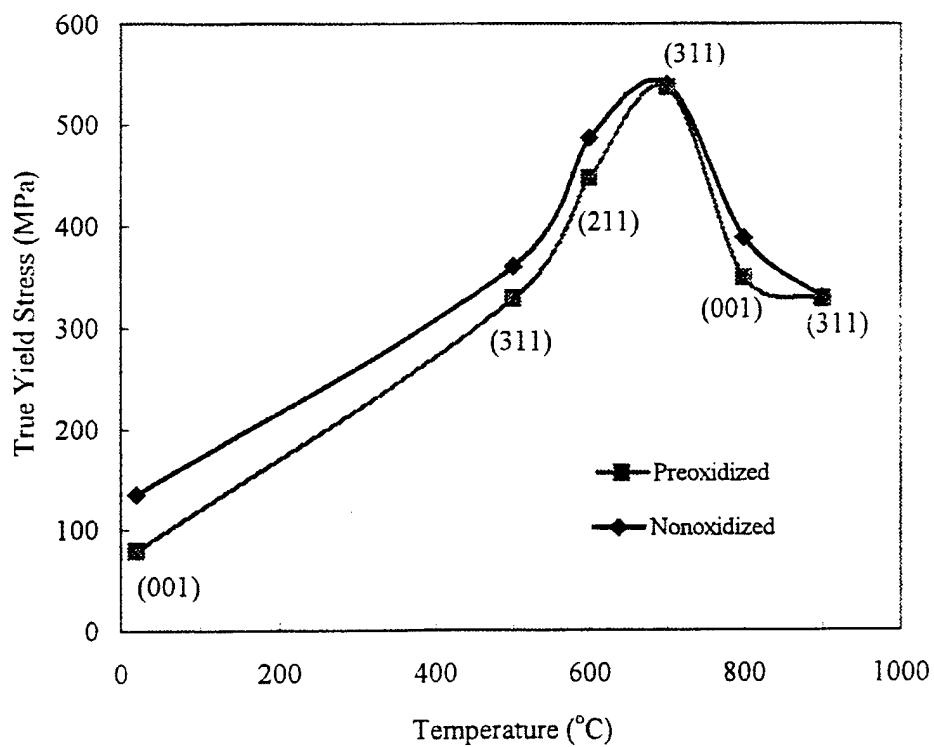
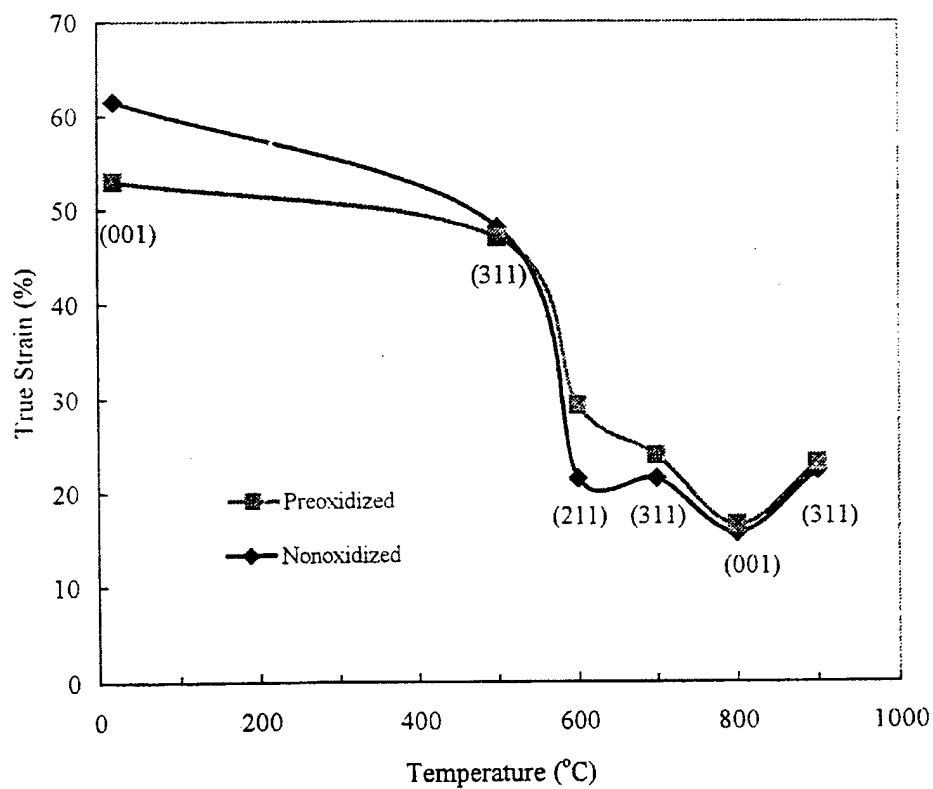**Figure 17. Yield stress of preoxidized and non-oxidized Ni₃Al single crystal vs temperature.**

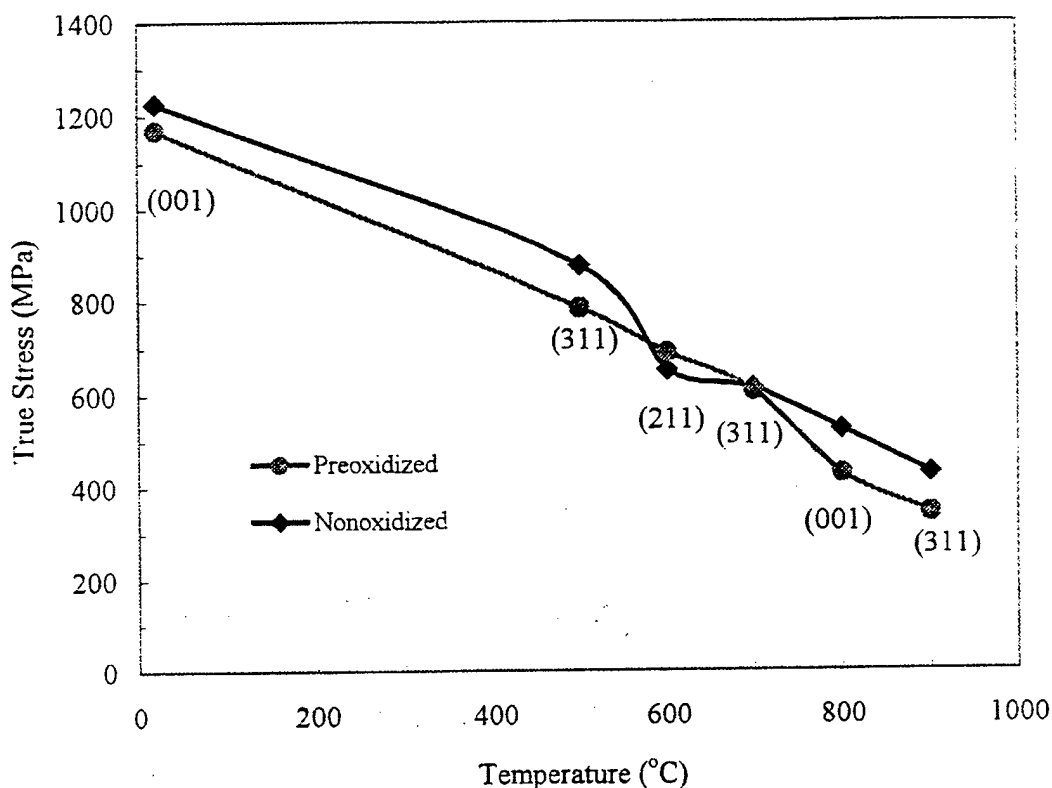**Figure 18. Elongation of preoxidized and non-oxidized Ni₃Al single crystal vs temperature.**

26

Figure 19. Ultimate stress of preoxidized and non-oxidized Ni₃Al single crystal vs temperature.

III.2.b. Molybdenum Based Alloys

Creep behavior of molybdenum based alloy single crystals at an elevated temperature ($\sim$0.6T$_m$) was examined in this study. Grain boundary sliding is absent in solution strengthened single crystalline alloys resulting in significantly reduced creep rates compared to their polycrystalline counterparts. Hafnium exhibits better strengthening effects in molybdenum relative to niobium due to the larger solute-solvent atomic size misfit in Mo-Hf compared to than in Mo-Nb. Dislocation climb and viscous drag are two competing processes during creep. The dominant creep mechanism depends on solute type, concentration and temperature. Results from this study confirm that the creep behavior in solution strengthened molybdenum single crystals corresponds to the Class II alloys as defined by Sherby and Burke. In addition, the creep response of these single crystals was found to be governed by the average nearest distance between the strengthening solute atoms in the lattice. Creep data show that the activation energy for creep contains two contributions: the normal diffusion energy and an additional solute-related energy which is proportional to the product (ne*c$^{1/3}$) where n is the stress exponent, e* is the atomic misfit factor and c is the atomic solute concentration. Results also indicate that for Mo-

27

Nb, there is a transition from class II to class I behavior at a Nb concentration of about three atomic percent.

Molybdenum-based alloy single crystals were prepared by using a high vacuum zone melting technique with an electron beam heating source. Orientations of the specimens used in creep testing were determined using the standard Laue back reflection method and results are given in Table 7. The specimens were cylindrical in shape measuring 7 mm in diameter and 12 mm in length. Due to the small size of the grown crystals, it is not feasible to conduct the high temperature creep tests in the tensile mode. Instead a Gleeble 1500 high temperature thermal mechanical testing system was used to evaluate the response of the crystals in the compressive mode. Compressive stress was applied in a hydraulic manner and the heating of the sample was accomplished by passing a direct AC heating current through the sample. The temperature and stress state of the sample were controlled automatically using the feedback loop of the control and data acquisition system. The error in the load is ± 5 kg which corresponds to a relative uncertainty of 3% at stress levels above 60 MPa. Creep rates at stresses below 10 MPa and at a temperature of 1850 K were extrapolated by assuming that the creep behavior obeys a power law within the stress range studied:

$$\dot{\varepsilon}_s = B \, \sigma^n = A \, \sigma^n \exp(-Q/RT) \tag{6}$$

where A and B are constants related to material parameters and creep conditions, σ is the applied stress in MPa, n is the stress exponent, T is the absolute temperature, Q is the activation energy of creep deformation and R is the gas constant.

For Mo and Mo-based alloys, Q has been previously determined for the polycrystalline structure and is on the order of 408 kJ/mole [24]. Stress exponents, n, for creep at 1850 K and at low stresses around 10 MPa for polycrystalline Mo were found to be in the range of 4.4 ~ 5.5. The creep rates are in the range of $10^{-6} \sim 10^{-7}$ s^{-1} [25-28] This corresponds to a class II materials according to the creep classification by Shelby. For modeling creep in Mo-based binary alloy single crystals, an activation energy of 413 kJ/mole was used in Equation 1, which is the average value of 408 kJ/mole obtained by Belomyttsev [24] and 418 kJ/mole obtained by Rhee [29]. Rhee [29] proposed that n for Mo-6%Nb was 3. Tachkova [30] presented that n for Mo with less than 1.8%Nb, the stress exponent was 5.8, and this exponent decreased to 3 when the Nb content was increased to 3%. Clearly, the creep mechanism in Mo-Nb alloys changes from 5 (class II) to 3 (class I) when the Nb content was higher than 3%. One of the objectives of this research is to determine the effects of solute additions on the creep mechanism in single crystalline molybdenum, especially the range of composition in which the molybdenum alloys behave as class II materials.

Table 7. Orientation of the Specimens in the Loading Direction.

Specimen ID	Composition	Axis Miller Index (hkl)
#2	Mo	Polycrystal
#8	Mo-2.4% Hf	Polycrystal
#13	Mo-14%Hf	Polycrystal
#3	Mo (unalloyed)	(0.12, 0.24, 1)
#6	Mo-0.95%Hf	(0.19, 0.38, 1)
#7	Mo-1.54%Hf	(0.10, 0.62, 1)
#9	Mo-3.0%Hf	(0.13, 0.17, 1)
#14	Mo-2.2%Nb	(0.05, 0.09, 1)
#15	Mo-12.5%Nb	(0.12, 0.52, 1)
#16	Mo-12.5%Nb	(0.02, 0.50, 1)

The log $\dot{\varepsilon}_S$ versus logσ plots for all the specimens are given in figure 20, where $\dot{\varepsilon}_S$ is the steady state creep rate at 1850 K and σ is the engineering stress in MPa. Creep rates of pure Mo were higher compared to both single crystalline alloys and polycrystalline alloys, indicative of the solute strengthening effect of Nb and Hf. It is also evident from the data that the strengthening effect of Hf (for example specimen #6, Mo-0.95%Hf) is greater then that of Nb (for example specimen #14, Mo-2.2%Nb). The n values (stress exponent which is related to the slope of the lines) of these specimen are different, indicating that different creep mechanisms are operative in these alloys.

The possible slip systems at high temperature for molybdenum single crystals were $\{101\}<\bar{1}11>$ [31], $\{211\}<\bar{1}11>$ [31] and $\{312\}<\bar{1}11>$ [30]. One of the issues is the effect of orientation on the observed creep response. The primary slip systems of the samples for compression test are considered to be those that have the greater Schmid's factors. The Schmid's factors of all specimen are listed in Table 8. The anticipated primary slip systems in each specimen are listed in Table 9. Multiple slip systems might be activated simultaneously for the specimens. According to the calculation, the maximum Schmid's factor for each specimen varied from 0.49 to 0.50, as indicated in Table 8. The effect of specimen orientation could therefore be ignored.
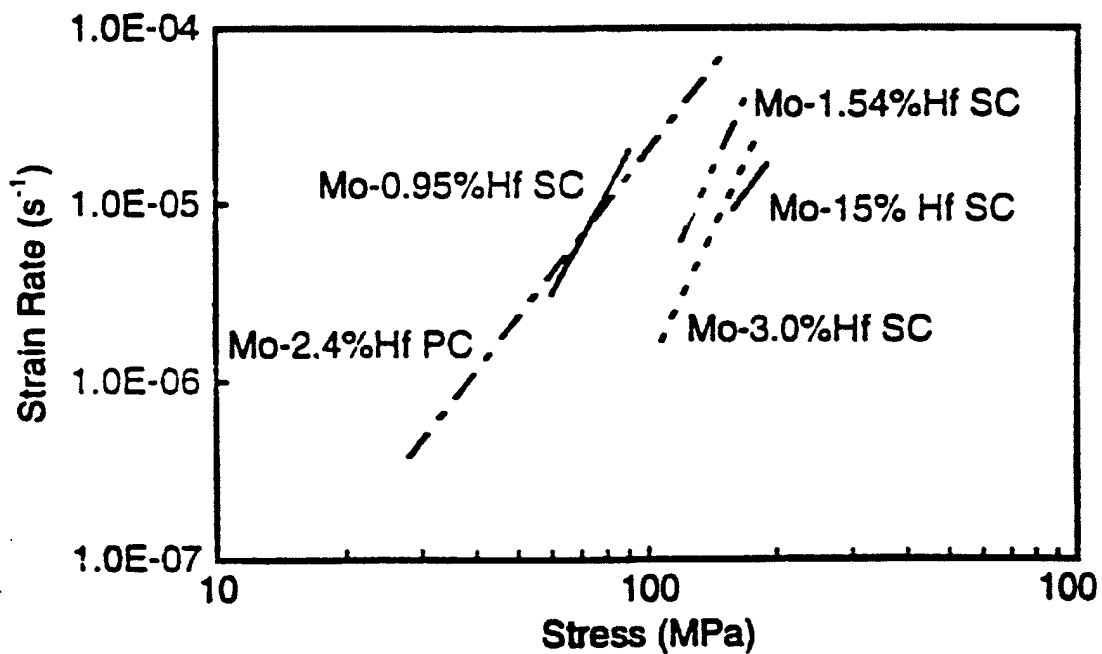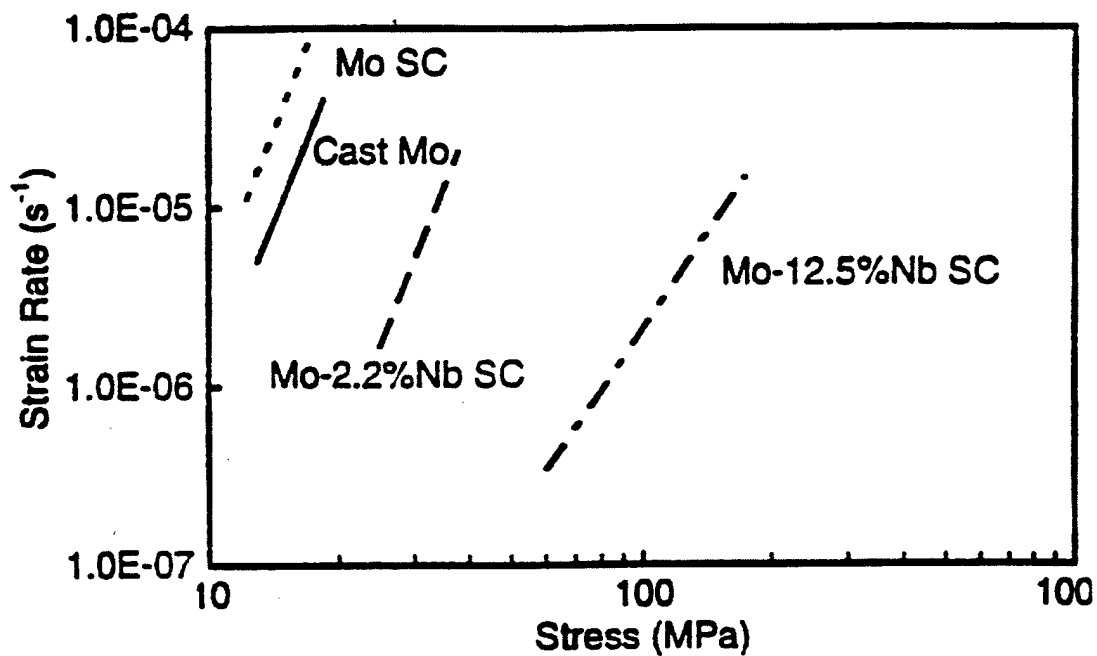
Figure 20. Stress dependence of creep rate at 1850K

At near $0.6T_m$, unalloyed molybdenum specimens recrystallize during high temperature creep testing due to a lack of strengthening sites. The deformation process occurs on highly available primary slip planes resulting in higher creep rates. Due to the experimental limitation and relatively high creep rates in pure Mo under this condition, only two data points were obtained at a stress level of 15 MPa. The experimental error was high and these data obtained should be used in comparison with other conditions and not be analyzed in absolute term. The steady state (or minimum) creep rates in the ten materials studied were analyzed using a least square fit method and results are summarized below:

#2 Mo, Polycrystal (PC)	$\dot{\varepsilon}_s = 5.8 \times 10^{-11} \times \sigma^{4.7}$ (s^{-1})	(7)
#8 Mo-2.4%Hf, P.C.	$\dot{\varepsilon}_s = 3.6 \times 10^{-12} \times \sigma^{3.4}$ (s^{-1})	(8)
#13 Mo-15%Hf, P.C.	$\dot{\varepsilon}_s = 3.0 \times 10^{-13} \times \sigma^{3.4}$ (s^{-1})	(9)
#3 Mo, S.C.	$\dot{\varepsilon}_s = 1.1 \times 10^{-10} \times \sigma^{4.7}$ (s^{-1})	(10)
#6 Mo-0.95%Hf, S.C.	$\dot{\varepsilon}_s = 1.3 \times 10^{-14} \times \sigma^{4.7}$ (s^{-1})	(11)
#7 Mo-1.54%Hf, S.C.	$\dot{\varepsilon}_s = 1.3 \times 10^{-15} \times \sigma^{4.7}$ (s^{-1})	(12)
#9 Mo-3%Hf, S.C.	$\dot{\varepsilon}_s = 5.6 \times 10^{-16} \times \sigma^{4.7}$ (s^{-1})	(13)
#14 Mo-2.2%Nb, S.C.	$\dot{\varepsilon}_s = 4.6 \times 10^{-13} \times \sigma^{4.7}$ (s^{-1})	(14)
#15,16 Mo-12.5%Nb, S.C	$\dot{\varepsilon}_s = 3.1 \times 10^{-13} \times \sigma^{3.4}$ (s^{-1})	(15)

Table 8. Schmid's Factors for Different Slip Systems

Specimen ID	Schmid's Factor for Slip Systems									
	[111]					[$\bar{1}$11]				
	($\bar{1}$01)	($\bar{2}$11)	($\bar{1}\bar{1}$2)	($\bar{3}$12)	($\bar{2}\bar{1}$3)	(101)	(211)	(1$\bar{1}$2)	(312)	(2$\bar{1}$3)
#3	0.46	0.30	0.49*	0.37	0.49*	0.48	0.36	0.46	0.42	0.48*
#4	0.44	0.30	0.47	0.40	0.48*	0.49*	0.41	0.44	0.46	0.47
#5	0.46	0.30	0.49*	0.37	0.49	0.46	0.30	0.49*	0.37	0.49*
#8	0.44	0.31	0.45	0.37	0.46	0.49*	0.42	0.43	0.46	0.47
#7	0.45	0.41	0.37	0.44	0.42	0.49*	0.47	0.38	0.49*	0.43
#19	0.44	0.27	0.50*	0.34	0.49*	0.46	0.34	0.46	0.39	0.47
#11	0.43	0.20	0.41	0.38	0.47	0.49*	0.45	0.40	0.48*	0.45
#14	0.44	0.26	0.49*	0.34	0.49*	0.44	0.29	0.48	0.44	0.48
#15	0.47	0.39	0.42	0.43	0.45	0.50*	0.47	0.42	0.50*	0.47
#16	0.49*	0.42	0.42	0.46	0.46	0.49*	0.43	0.42	0.48*	0.46

* Indicates the maximum value of Schmid's factor.

Table 9. The Primary Slip Systems in Different Specimens

Specimen ID	Primary slip systems	
	[111]	[$\bar{1}$11]
#3	($\bar{1}$12), ($\bar{2}$13)	(2$\bar{1}$3)
#4		(101), (2$\bar{1}$3)
#5	($\bar{1}$12)	($\bar{1}$12), (2$\bar{1}$3)
#6		(101), (2$\bar{1}$3)
#7		(101), (2$\bar{1}$3), (211)
#9	($\bar{1}$12), ($\bar{2}$13)	
#11		(101)(312)
#14	($\bar{1}$01)	(312)
#15		(101),(312)
#16	($\bar{1}$01)	(101)(312)

A comparison of Equations 2 to 10 with the basic form of creep given in Equation 6 indicates that the creep constant B is reduced due to the presence of strengthening solute. The absence of grain boundary in single crystals enhances the creep rate relative to its polycrystalline counterpart by a factor of two. This indicates that grain boundary sliding is not an important creep mechanism in this material, and creep in single and polycrystalline molybdenum is essential the same. The small difference is due to the crystallographic orientation of the single crystal (Schmid's factor) and the random texture of the polycrystalline specimens.

Creep results show that Hf is a more effective strengthening agent than Nb in molybdenum. Specimen #6 contains 0.95% Hf but shows a lower creep constant compared to that of specimen #14 with 2.2%Nb. More effective strengthening effect of Hf was attributed to its larger atomic-size difference relative to the solvent molybdenum matrix resulting in an increase in the activation energy for creep deformation. The observed strengthening effect is also related to the concentration of the solutes in the alloy.

In Mo-based dilute single crystalline alloys, the n values are all near 4.7. This indicates that creep in these dilute alloy single crystals is of the class II type dominated by dislocation climb. This is of course limited to the temperature and stress range examined. As shown in Figure 21 (and Equations 7-15), lower creep rates can be achieved by increasing the Hf concentration. A similar trend was observed in Mo-Nb. An analysis of the creep data was conducted in terms of the solute type and solute concentration as outlined below.
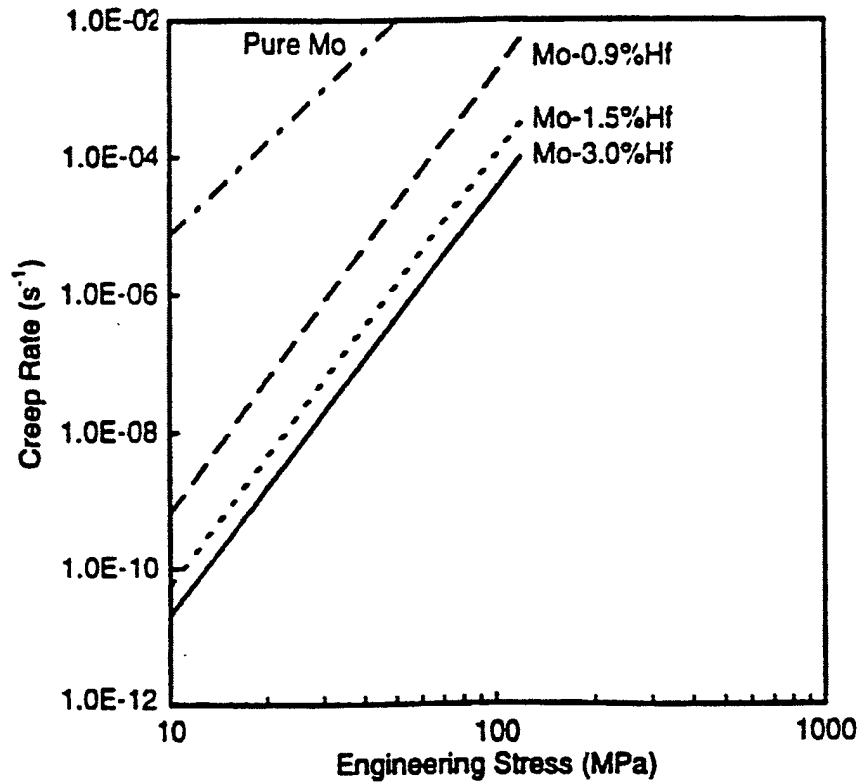
Figure 21. Enhancement in creep resistance with increasing Hf content.

According to the results shown in this study, Mo-Nb and Mo-Hf alloys with high concentrations of solute behave like a class I material. However, at low solute contents, alloy single crystals of these systems exhibit class II creep behavior dominated by dislocation climb. The transition occurs at about 2 to 3 atomic percent. This process is controlled by the multiple slip systems and the formation of dislocation network during creep deformation. The extra activation energy E is considered to be proportional to the average nearest distance between the solute atoms in the lattice space. Therefore, the concentration of solute should affect the creep rate in terms of $c^{1/3}$. According to the creep model proposed by Gao et al [32], steady state creep in such alloys can be expressed in the following manners:

$$\dot{\varepsilon}_{s,alloy} = \dot{\varepsilon}_{s,pure} \exp(-K\,n\,e\,c^{1/3}/RT) \tag{16}$$

where $\dot{\varepsilon}_{s,\,alloy}$ and $\dot{\varepsilon}_{s,\,pure}$ are respectively the steady-state creep rates for the alloy and the pure metal, K is a material constant which depends only on the matrix structure (a constant in Mo alloys independent of solute type), n is the stress exponent for the creep process, e is the lattice strain generated by the solute in the matrix, c is the atomic concentration of the solute of interest, R is the gas constant, and T is the absolute temperature. In this model, the presence of alloy

33

atoms introduces extra energy for dislocation climb. These solute atoms act as obstacles resulting in an additional activation energy, ΔE, for creep to the alloy. In order to verify these models, the creep data of Mo-Hf alloys were fitted with both $c^{1/3}$ and $c^{1/2}$ as proposed by Gao [32]. The comparison of the fitting at 10 MPa is given in figures 21 and 22. Results show that $c^{1/3}$ provides a better fit to the data than the $c^{1/2}$ approach suggesting that the strengthening is to the solute atoms acting as obstacles for dislocations (the parameter $c^{1/3}$ is related to the mean distance between solute atoms). This observation indicates that the extra energy ΔE is associated with the average distance between solute atoms in space.

In addition, the energy ΔE is also proportional to the atomic misfit between the solute and the solvent atoms. This misfit is accounted for by the e term in Equation 16, can be expressed in terms of the atomic size mismatch between the solute and solvent size (e) or the effective atomic size difference (e*). The parameter e is defined as $|r_{alloy}-r_{pure}|/r_{pure}$ where the two r's are the effective radii of the atom in the alloy and pure molybdenum. Oikawa and Langdon [33] has defined the parameter e* as $(\Omega^*_B/\Omega_A)^{1/3}-1$, where Ω_B^* is the effective atomic volume of solute atoms in the alloy, and Ω_A is the atomic volume of solvent. The values of e and e* for the two alloys are given in Table 10.

Table 10. The Values of e* and e for the Two Mo Alloys

Alloys	e* (from ref 14)	e
Mo-Hf Alloy	0.0794	0.137
Mo-Nb Alloy	0.0409	0.046

Using creep data (from the present study together with information in the available literature) with the appropriate e and e* values shown in Table 10, the dependence of the creep rate at the stress range of 10 to 170 MPa at 1850 K for Mo-Hf and Mo-Nb was determined to be, Using e:

$$\dot{\varepsilon}_{s,\text{Mo-Hf alloy}} = \dot{\varepsilon}_{s,\text{pure}} \exp(-210000 \ n \ e_{Hf} \ c^{1/3}/RT) \qquad (17)$$
$$\dot{\varepsilon}_{s,\text{Mo-Nb alloy}} = \dot{\varepsilon}_{s,\text{pure}} \exp(-210000 \ n \ e_{Nb} \ c^{1/3}/RT) \qquad (18)$$

and using e*:

$$\dot{\varepsilon}_{s,\text{Mo-Hf alloy}} = \dot{\varepsilon}_{s,\text{pure}} \exp(-360000 \ n \ e^*_{Hf} \ c^{1/3}/RT) \qquad (19)$$
$$\dot{\varepsilon}_{s,\text{Mo-Nb alloy}} = \dot{\varepsilon}_{s,\text{pure}} \exp(-360000 \ n \ e^*_{Nb} \ c^{1/3}/RT) \qquad (20)$$

Notice that in this formulation, the constant K is the same for the two alloy systems but are

allowed to vary between the use of e versus e*. An analysis was conducted to compare the fitting of the two approaches using e and e* to the experimental data. Results, shown in figures 22 and 23, clearly indicate that the e* parameter offers a more satisfactory fit to the data. According to this analysis, creep of dilute binary Mo-based alloys exhibiting class II behavior can be predicted by introducing an additional energy barrier with a magnitude of $360,000ne*c^{1/3}$. This additional energy barrier results in a reduction in creep rate according to exp(- E/RT) relative to the unalloyed pure material.

In polycrystalline alloys (#8 and #13), the n value is 3.4 indicating that creep deformation is dominated by grain boundary sliding which is faster than the dislocation climb and the dislocation viscous drag process. The creep behavior for grain boundary sliding has been modeled by Langdon [34] as:

$$\dot{\varepsilon}_{s,gbs} = A(b/d)^2(\sigma/G)^{3.5} \qquad (21)$$
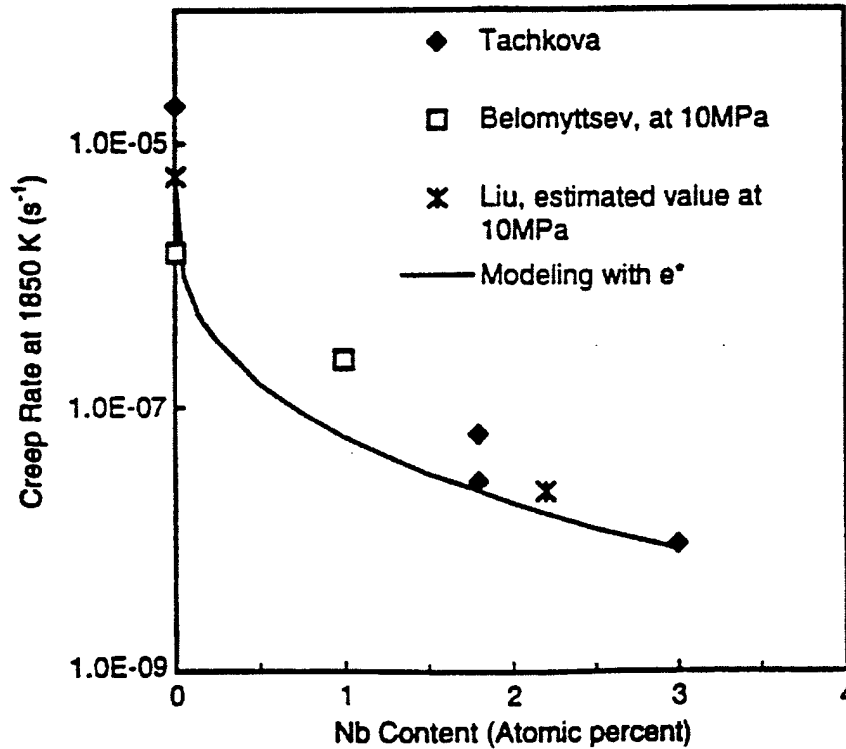

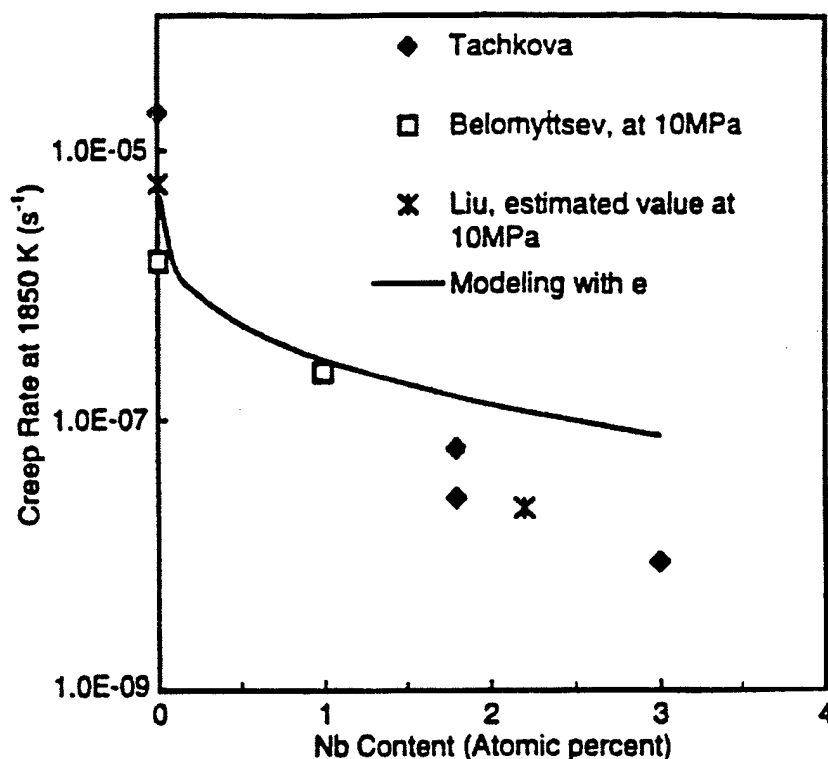Figure 22. Fitting of the creep data of Class II alloys of Mo-Nb using the parameter e* according to Equation 20.

Figure 23. Fitting of the creep data of Class II alloys of Mo-Nb using the parameter e according to Equation 18.

where G is the shear modulus and A is a function of stress concentration, triple point geometry, Burgers vector, dislocation sources, shear modulus, diffusion coefficient, grain size and Boltzmann thermal energy. A is a dimensionless constant. Based on the above equations, the creep rate is inversely proportional to $d^{1\sim2}$. The strengthening effects heavily depends on the grain sizes. It is evident that the absence of grain boundaries in the single crystal structure significantly alters the creep mechanism resulting in higher stability.

Binary single crystalline Mo-Hf and Mo-Nb alloys possess significantly reduced creep rates relative to the pure crystals and their polycrystalline counterparts. The strengthening effect of solute depends on atomic size difference e* and the concentration. At solute concentrations below 3 atomic percent, the creep behavior corresponds to that of Class II type alloys and is governed by the average nearest distance between the solute atoms in the lattice space. A model based on the presence of an additional activation energy for creep (ΔE) is used successfully to explain the creep rates observed. The energy ΔE is proportional to the product of $(Kne*c^{1/3})$, where K equals to 360 kJ/mole for both alloy systems. The creep behavior in the alloys in the polycrystalline state was found to be quite different than that in dilute single crystals. Grain boundary sliding dominates in the polycrystalline alloys resulting in higher creep rate and a lower stress exponent.

III.2.c. Tungsten Based Alloys

Mechanical properties of the crystals (both the alloy and unalloyed tungsten together with their polycrystalline counterparts) were determined as a function of temperature. Table 11 shows the test matrix employed. The strain rate change method was employed for most of the tests in order to acquire the maximum amount of data from the limited number of specimens. Figure 24 shows a representative plot for such a strain rate change test taken at 1873K for a W-Ta alloy with an axial direction of [001]. The creep data obtained are summarized in figure 25 showing the enhancement of creep resistance due to the addition of Ta in single crystalline tungsten. This summary shows that the creep rates of the alloy are more than three orders of magnitude lower than the unalloyed crystals. A modeling study (similar to that presented in the molybdenum case) was conducted and results show that the strengthening effect of Ta can also be explained by the proposed mechanism (see last section).

Table 11. Summary of Mechanical Property Tests Conducted*

Test Temp	Strain Rates (given in $\dot{\varepsilon}$) and Orientations (given in [hkl])			
	Tungsten Polycrystal	W-Ta Polycrystal	Tungsten Single Crystal	W-Ta Single Crystal
Room				$\dot{\varepsilon} = 10^{-4}\,s^{-1}$ [001], [011]
1000°C	$\dot{\varepsilon}=10^{-4}s^{-1}$ $\dot{\varepsilon}=10^{-6}\text{-}10^{-3}s^{-1}$	$\dot{\varepsilon}=10^{-4}s^{-1}$ $\dot{\varepsilon}=10^{-6}\text{-}10^{-3}s^{-1}$	$\dot{\varepsilon}=10^{-4}s^{-1}$ [111] $\dot{\varepsilon}=10^{-6}\text{-}10^{-3}s^{-1}$ [111]	$\dot{\varepsilon} = 10^{-4}s^{-1}$ [001], [111]
1200°C	$\dot{\varepsilon}=10^{-4}s^{-1}$	$\dot{\varepsilon}=10^{-3}s^{-1}$ $\dot{\varepsilon}=10^{-6}\text{-}10^{-3}s^{-1}$	$\dot{\varepsilon}=10^{-6}\text{-}10^{-3}s^{-1}$ [001], [111]	$\dot{\varepsilon}=10^{-6}\text{-}10^{-3}s^{-1}$ [001], [111]
1400°C	$\dot{\varepsilon}=10^{-6}\text{-}10^{-3}s^{-1}$	$\dot{\varepsilon}=10^{-6}\text{-}10^{-3}s^{-1}$	$\dot{\varepsilon}=10^{-6}\text{-}10^{-3}s^{-1}$ [001], [111]	$\dot{\varepsilon}=10^{-6}\text{-}10^{-3}s^{-1}$ [001], [111]
1500°C	$\dot{\varepsilon}=10^{-4}s^{-1}$ $\dot{\varepsilon}=10^{-3}s^{-1}$	$\dot{\varepsilon}=10^{-4}s^{-1}$ $\dot{\varepsilon}=5\times10^{-4}s^{-1}$ $\dot{\varepsilon}=10^{-3}s^{-1}$	$\dot{\varepsilon}=10^{-6}\text{-}10^{-3}s^{-1}$ [001], [111]	$\dot{\varepsilon}=10^{-6}\text{-}10^{-3}s^{-1}$ [001], [111]
1600°C			$\dot{\varepsilon}=10^{-6}\text{-}10^{-3}s^{-1}$ [001], [111]	$\dot{\varepsilon}=10^{-6}\text{-}10^{-3}s^{-1}$ [001], [111]

*Two types of mechanical testing were conducted: constant strain rate and strain rate change. In the latter case, the strain rates were increased in the range from 10^{-6} to $10^{-3}s^{-1}$.
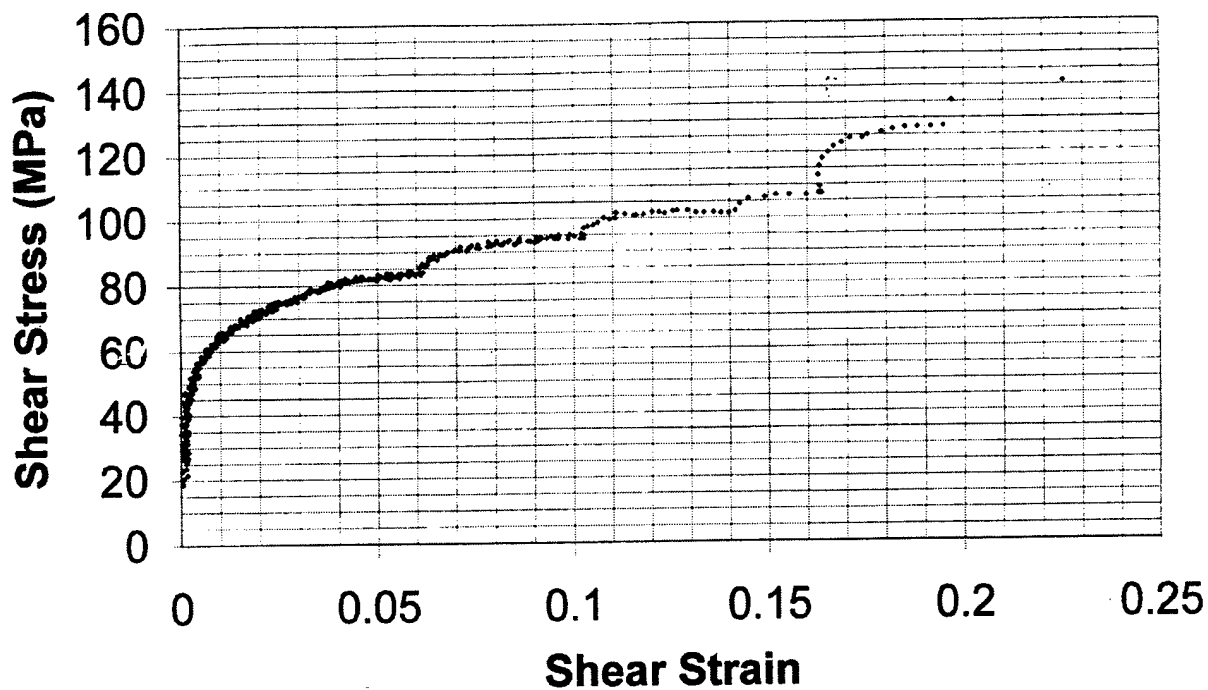
Figure 24. Stress-strain data for a W-Ta single crystal tested at 1863K with changing
strain rates of 10^{-6}, 2×10^{-6}, 5×10^{-6}, 10^{-5}, 10^{-4}, 10^{-3} s^{-1}.
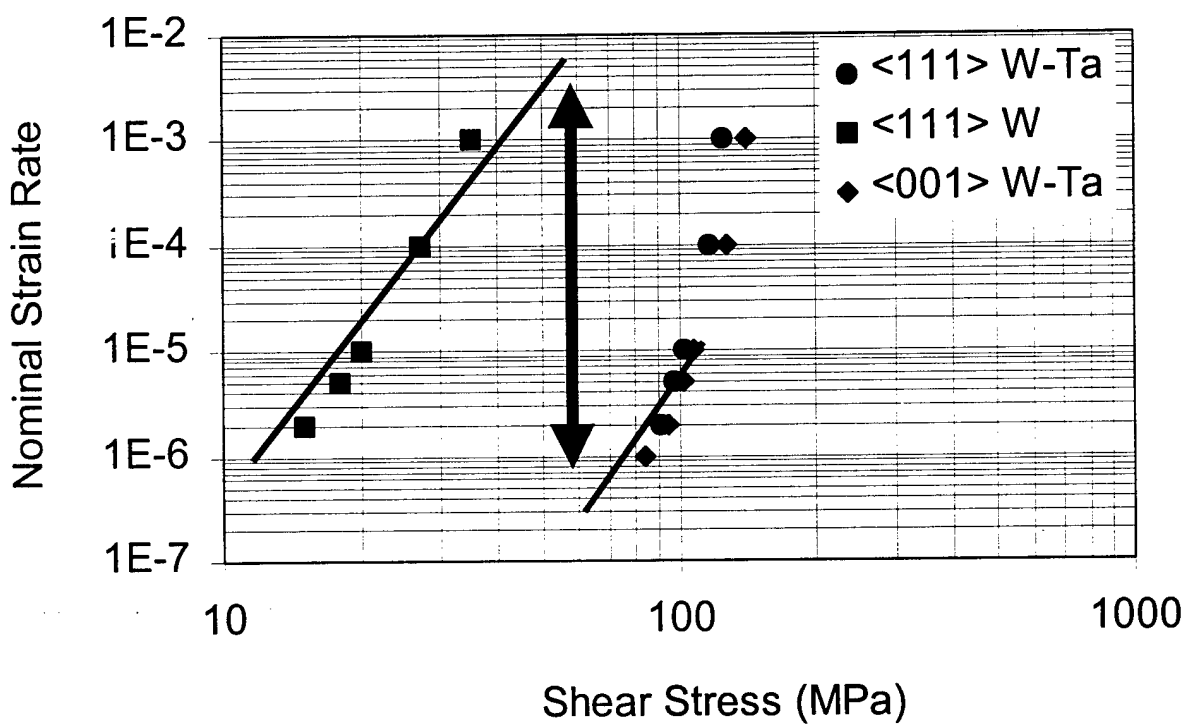

Figure 25. Summary of creep data showing the enhancement of creep resistance in the
W-Ta alloycompared to unalloyed tungsten

III.3. Joining

Joining of refractory metals has been an important part of the project. Joining is required for initial fabrication (since refractory metals are difficult to form to near-net shape) and for bonding refractory metals to other high-temperature materials (*e.g.* structural intermetallics or graphite, of which the former was examined in the project). If the industrial application of refractory metals is to increase then joining will be required for both pre-service (*e.g.* casting defects) and post-service (*e.g.* thermal fatigue cracks) repair.

Work on the joining of refractory metals has focused on the use of transient liquid phase (TLP) bonding. TLP bonding employs a liquid forming interlayer, like brazing. However, interdiffusion between the interlayer and the substrates, during bonding, has the effect of inducing isothermal-solidification at the bonding temperature. Given a suitably prolonged post-isothermal-solidification homogenization treatment bonds with microstructures, remelt temperatures and mechanical properties similar to the parent materials can be produced. Although diffusion bonds can also possess parent metal microstructures and properties, TLP bonding (as a capillary joining process) offers a far greater degree of geometrical freedom in joint design. Also, in cases where refractory metals are to be joined to other materials (*e.g.* aluminide intermetallics) with highly stable oxide layers on the faying surfaces, TLP bonding has a clear advantage over diffusion bonding. Diffusion bonding of metallic materials is crucially dependent on the establishment of metal to metal contact at the bond-line and this is not possible when continuous, stable oxide layers are present on the faying surfaces. In contrast, in TLP bonding, faying surface oxide layers can be undermined, reduced and/or dissolved by constituents of the interlayer (or by liquid oxides formed on some interlayers). Compared with fusion welding, TLP bonding is a much less aggressive process and is therefore well suited to damage sensitive materials, such as refractory metals.

Work conducted under the project has focused on the joining of polycrystalline commercially-pure molybdenum substrates. The intent in this work was to develop TLP bonding strategies using readily available and low cost polycrystalline material. However, the TLP bonding techniques developed in this work are also well suited to use with single crystal substrates and also to other refractory metals, such as tungsten. The primary objective of the work on joining has been to develop techniques for bonding molybdenum to molybdenum. However, a limited amount of research has also been undertaken on the joining of molybdenum to structural intermetallic compounds.

During the initial stages of the project, a TLP bonding strategy that employed commercially pure titanium as an interlayer was investigated for Mo – Mo joining. The advantage of using pure titanium lies in the formation of a β–(Ti,Mo) body centered cubic solid solution (figure 26), rather than undesired intermetallics, even if several atomic percent of titanium remains present. In this case, once sufficient interdiffusion has occurred between the

interlayer and the substrates, a continuous BCC solid solution will be present right across the bond-line. Work conducted under this project indicated that β–(Ti, Mo) did indeed form readily at the bond-line of Mo/Ti/Mo bonds held at 1700 °C. However, a relatively prolonged bonding time was required to prevent entirely the formation of HCP α–Ti. This bonding time will be of the order of tens or hundreds of hours, depending on the initial interlayer thickness (say from 10 to 100 μm), since the interlayer thickness governs the amount of titanium that must be diffused to bring the center-line composition within the solubility of Ti in Mo. These bonding times are somewhat longer than would be desired, however, they do remain feasible industrially, especially if thin titanium interlayers were employed. Furthermore, wettability in the Mo/Ti/Mo bonds was excellent and pore-free joints are produced. Also, although this process was developed for polycrystalline molybdenum substrates, it is equally applicable to single-crystal molybdenum or tungsten (the latter in either single-crystal or polycrystalline forms). However, the use of pure titanium interlayers does have a major disadvantage, namely that the melting temperature of pure titanium (1670 °C) is well above the capability of commercial vacuum
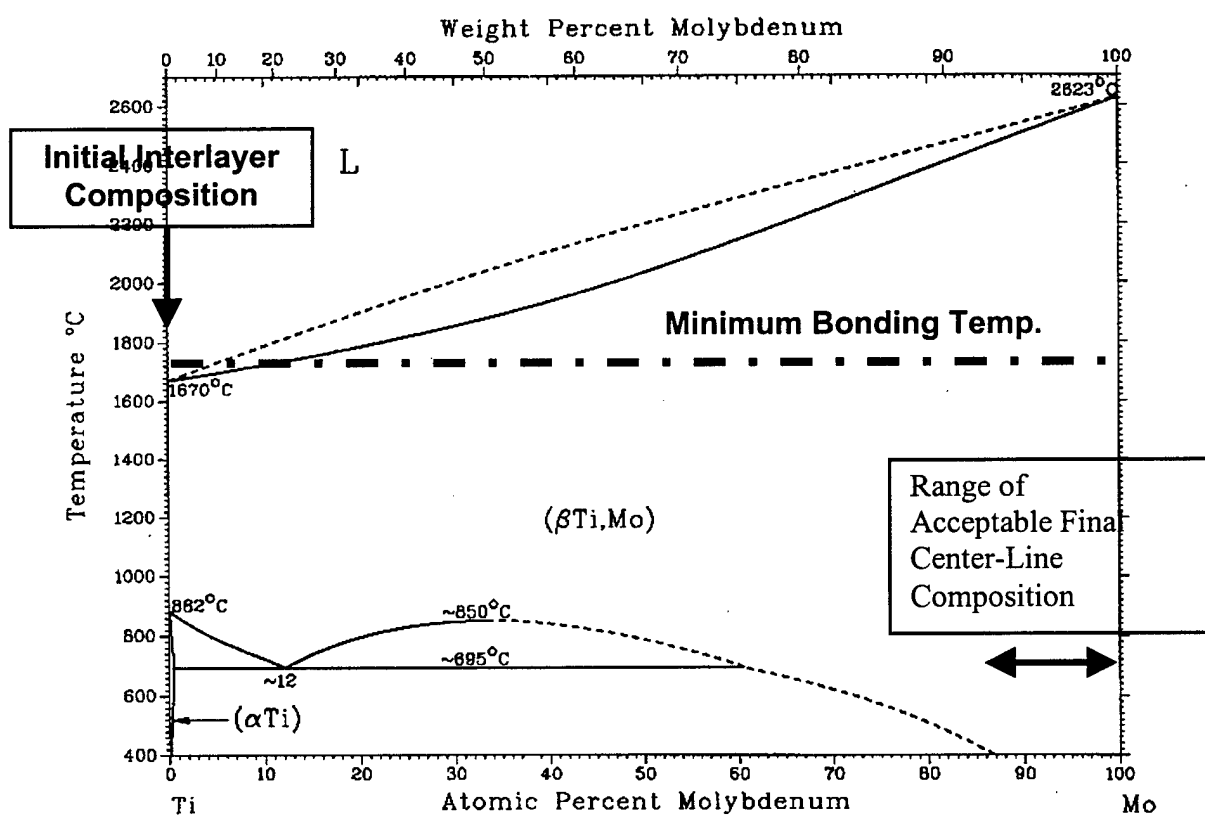

Figure 26. The Ti – Mo binary phase diagram [35]. The initial interlayer and acceptable final center-line compositions and the minimum bonding-temperature used with pure titanium interlayers are marked on the diagram.

40

brazing furnaces. Thus, the high bonding temperature that is required when pure titanium interlayers are used limits the commercial application of this approach to vendors with specialized high-temperature vacuum furnaces. Thus, an effort was made to identify alternative strategies for TLP bonding refractory metals.

In a different approach, the use of commercial Ni – 4.5 wt. % Si – 3.2 wt. % B (designated by the American Welding Society as BNi–3) foil interlayers has been investigated. These have the advantage that a low interlayer melting temperature allows bonding at only 1065 °C. However, molybdenum is a stable boride and silicide former and there are numerous different intermetallics in the Ni – Mo system. Thus, the production of fully homogenized joints is challenging (and probably impracticable). Nonetheless, results from the project suggest that the formation of undesirable intermetallics in these bonds is manageable to some extent. Note, an alternative considered was the use of Fe – Si – B interlayers. However, this was rejected due to the risk of the formation of the highly embrittling σ–FeMo phase.

In response to the problems with joining molybdenum using either pure titanium or commercial interlayers for high-temperature materials, the PIs have sought to develop an alternate TLP bonding strategy for joining polycrystalline molybdenum. The aim of this activity has been to substantially reduce the bonding temperature, whilst keeping the advantages of the titanium interlayer approach. As in other work, attention has focused on polycrystalline molybdenum substrates, however, as before, this work should also be applicable to single-crystal molybdenum and polycrystalline or single-crystal tungsten. In selecting an interlayer material, the following criteria were used:

- The major constituent of the interlayer should have a high solubility in the substrate.

- The interlayer should form a deep eutectic to allow the use of a low bonding temperature (preferably not above 1150 °C).

- Systems forming very stable intermetallics should be avoided.

An extensive examination of binary and ternary phase diagrams was made, based on the three criteria listed above. In searching for a suitable alternative to pure titanium, it became clear that the most promising route was to employ a binary alloy consisting of titanium, plus a melting-point depressant. Ideally, this melting-point depressant would have been highly soluble in the molybdenum substrates, but a suitable candidate could not be found. Instead, nickel was used as a melting point depressant to form a binary alloy with a composition of Ti – 25 at. % Ni. Nickel forms a series of intermetallics with molybdenum and this alloy was the lowest nickel composition at which a reasonable brazing temperature (1150 °C or below) could be obtained. Although the Ti – Ni system is perhaps best known for the NiTi shape memory alloy, the region of interest in the present work was the Ti – Ti_2Ni eutectic found at the titanium-rich end of the phase diagram (figure 27).
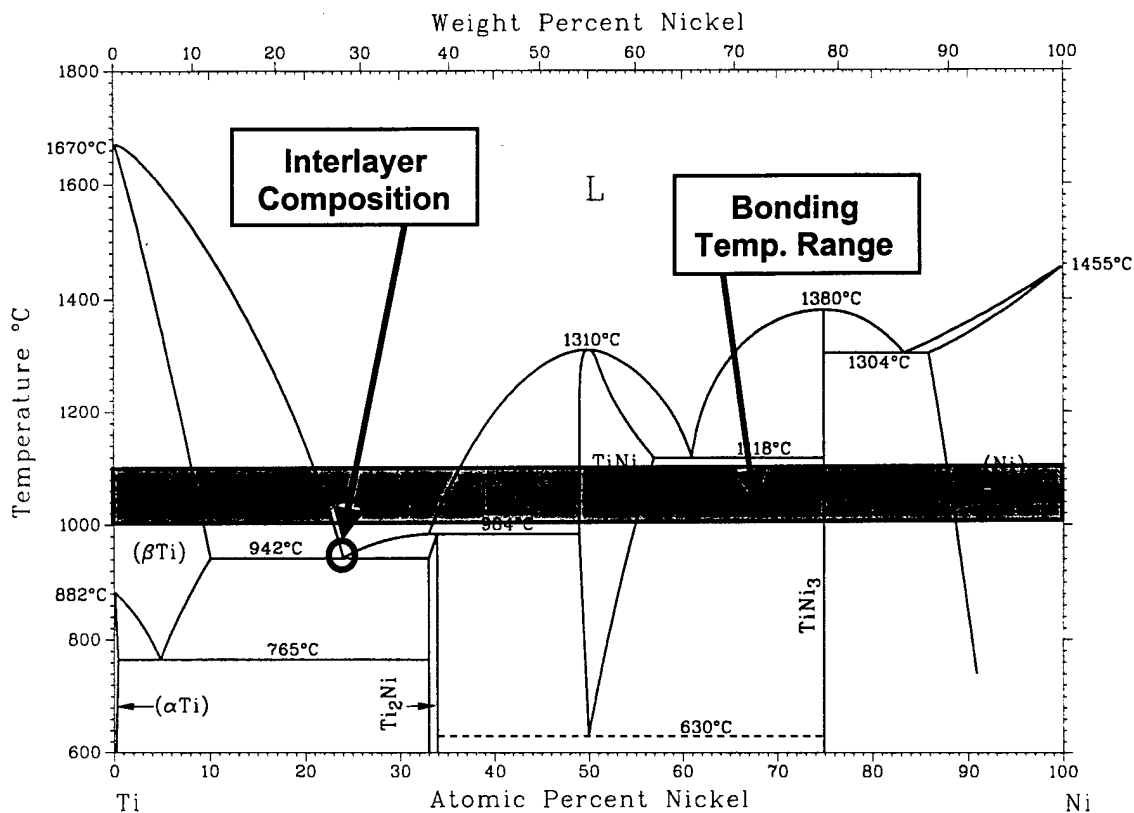
41

Figure 27. The Ti – Ni binary phase diagram [35]. The composition selected as an interlayer material and the range of required bonding temperature are marked.

Use of the Ti – Ti₂Ni system makes a bonding temperature in the 1000 – 1100 °C range practicable. The nickel solubility in molybdenum is very limited (see figure 28 for the Mo – Ti – Ni ternary system). Thus the use of a relatively low nickel interlayer is important (common interlayers for TLP bonding of high-temperature materials are nickel-based). Suitable Ti – Ni foils are not available commercially and hence these have been produced in-house from an arc melted precursor.
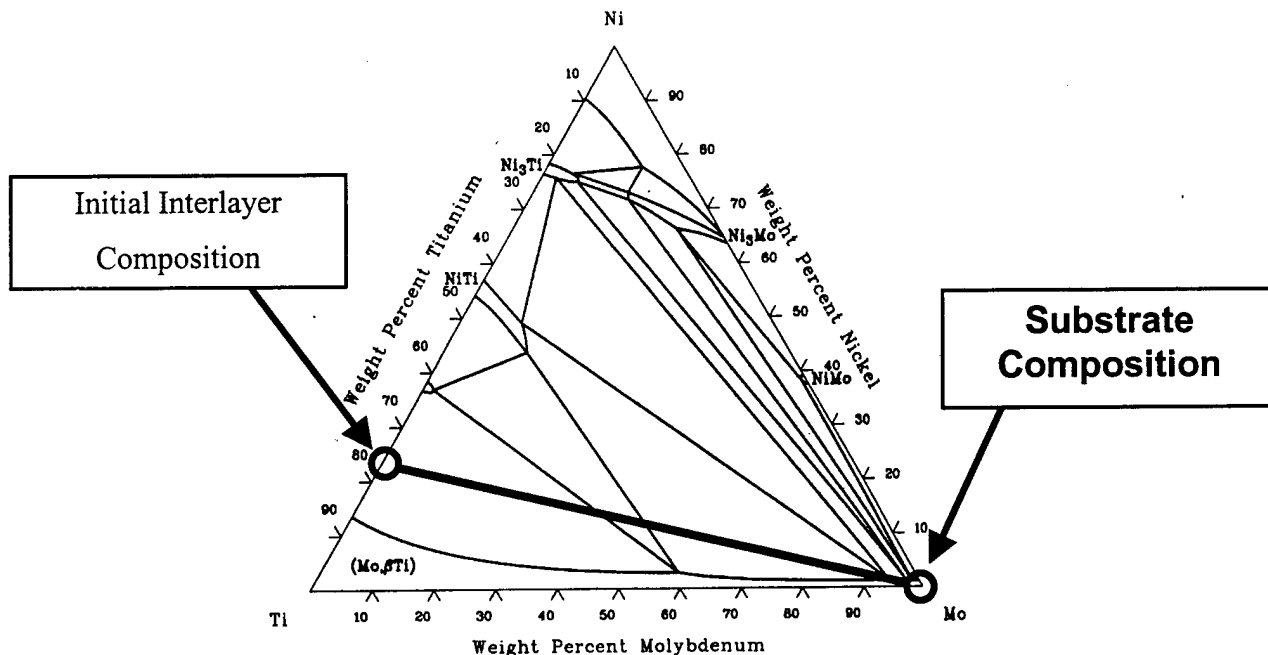
**Figure 28. Isothermal Section at 900 °C of the Mo – Ti – Ni ternary phase diagram [36].
The initial composition of the Ti – Ni interlayer and that of the substrate are indicated.**

Following production of the Ti – Ni alloy by arc melting and after homogenization this material was first slit and then ground to produce interlayers with thicknesses in the range of 50 – 100 μm. Bonding was conducted under a 10^{-5} torr, or better, vacuum at a temperature of 1050 °C. Bonding times ranging from zero (*i.e.* heat to the bonding temperature and then immediately cool) up to 150 hours were examined. A variety of post-bond heat-treatments with durations of up to 1ₒ0 hours at 1350 °C were investigated. Bonds were characterized by light microscopy, scanning electron microscopy and energy dispersive X-ray spectroscopy. Figure 29 shows a typical as-bonded sample; compare this with figure 30, which shows a similar bond after a post-bond heat-treatment.

Initial results with the Ti – Ni interlayer were promising. An Mo – Ti solid-solution grew from the substrates into the joint (figure 29) and the eutectic was gradually removed. However, bonding times were fairly protracted with at least 20 hours at 1000 °C being required to complete isothermal solidification for interlayers with initial thicknesses in the 50 to 100 μm range. Further thermal exposure was then needed to complete homogenization. In case of the Ni – Ti interlayers, the main problem was expected to be the bond-line nickel, since this has a low solubility in molybdenum. Thus, it was necessary to reduce the bond center-line nickel content if the formation of nickel – molybdenum intermetallics was to be avoided. It was found that even prolonged holding at the 1050 °C bonding temperature was found to leave nickel-bearing intermetallics at the bond-line. However the nickel-bearing intermetallics were removed by

43

means of a post-bond heat-treatment at 1350 °C. Indeed, a combination of diffusion of molybdenum from the substrates into the bond-line and diffusion of nickel in the opposite direction left little detectable nickel at the bond center-line after a 100 hour at 1350 °C post-bond heat-treatment. Far better results were obtained using the Ti – Ni interlayers than in the case of commercial nickel-base brazing foils. In the latter case, not merely did extensive formation of Ni – Mo intermetallics take place, but also thick layers of stable molybdenum borides and silicides were produced.

In contrast to the ease with which the (relatively limited) amount of nickel present in the bonds was diluted, the bond-line and adjacent substrates tended to remain titanium-rich after bonding. Body centered cubic (BCC) molybdenum and the BCC β-titanium phase have complete mutual solubility. However, at low temperatures, pure titanium forms a hexagonal phase (α–Ti). In molybdenum-rich systems, a BCC β–(Mo, Ti) solid-solution is produced at all temperatures, whereas in systems containing greater amounts of titanium a two phase $\alpha + \beta$ mixture is present at low temperatures and single phase β is only observed at high temperatures.
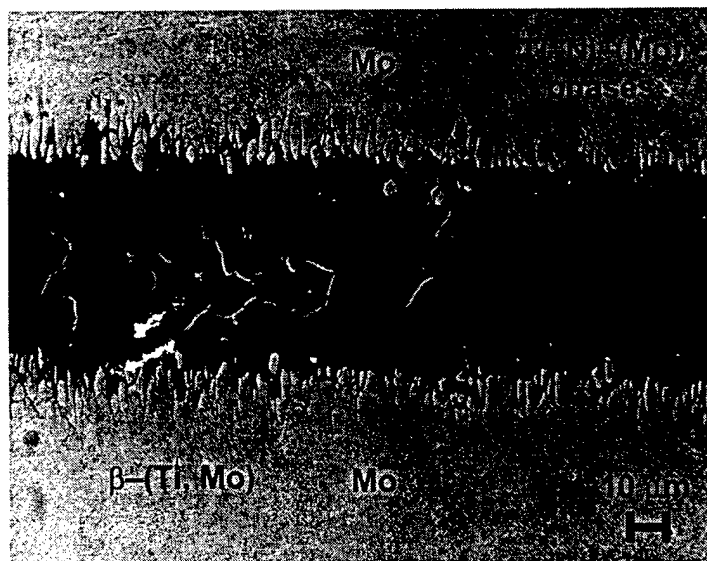

Figure 29. Microstructure of an Mo / Ti – Ni / Mo bond held for 20 minutes at 1,050 °C. Notice the presence of large regions containing a variety of intermetallics bearing Ti, Ni and/or Mo. Compare this with figure 30, which shows the effect of post-bond heat-treatment at 1350 °C for 100 hours.

In bonds subjected to post-bond heat-treatment at 1350 °C for 100 hours or more, the bond-center line was found to consist largely of single-phase β–(Mo, Ti). However, some precipitation of α–Ti was present at β – β grain boundaries and occasional intragranular α–Ti deposits were observed (one of these can be seen in figure 30). Although this α–Ti precipitation is not desired, the presence of this phase has far less damaging implications for bond mechanical properties than would the presence of brittle (nickel-bearing) intermetallics. Isothermal solidification of the bonds proceeds by epitaxial growth of β–(Mo, Ti) from the Mo substrates. Consequently, with the exception of the α–Ti precipitates discussed above, the bond-line was microstructurally similar to the bulk Mo substrates.
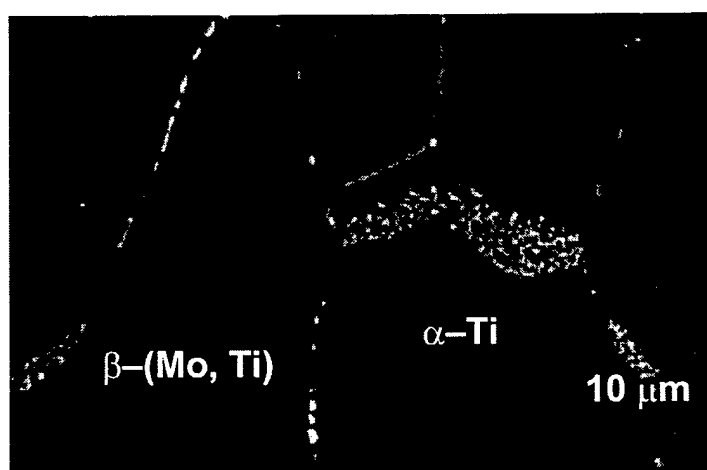
Figure 30. Microstructure of an Mo / Ti – Ni / Mo bond held for 20 minutes at 1,050 °C and then heat-treated for 100 hours at 1,350 °C. Notice that no nickel-bearing intermetallics can be observed within the bond, although some deposits of α–Ti remain present.

In summary, although the resulting bond-line microstructures are not completely identical to the bulk substrates, the use of Ti – Ni interlayers appears to be an attractive route for TLP bonding Mo using conditions that are attainable in commercial vacuum brazing furnaces. There is scope in any future project for decreasing the bonding time required when Ti – Ni interlayers are employed. Possible strategies to achieve this goal include the following:

- Use of relatively thin (< 50 μm) Ti – Ni interlayers. This offers fairly easy control over microstructural development. However, the Ti – Ni interlayers are quite brittle and hence the scope for the production of thin interlayers is limited.

- Reaction of pure nickel and titanium foils (as an Ni/Ti/Ni sandwich) to produce the Ti – Ti$_2$Ni eutectic *in-situ*. This approach allows the use of relatively thin interlayers (5

to 10 μm in total), but will complicate microstructural development.

- A significant applied load could be employed with standard (~ 50 μm) interlayers to extrude out excess liquid and hence decrease bonding times. This approach should be easy to implement in the lab., but is not applicable to all commercial joint geometries.

In addition to work on the TLP bonding of Mo – Mo, the joining of Mo to the structural intermetallic NiAl has been investigated to a limited extent. For this Mo – NiAl joining work, a different approach has been employed. Here, no interlayer was used, as a liquid is formed *in-situ* by virtue of the formation of an NiAl – Mo eutectic. The intent of this work is not to achieve isothermal solidification. Instead, a layer of NiAl – Mo eutectic is left at the bond-line for the following reasons:

- the presence of this layer will provide an intermediate coefficient of thermal expansion (CTE) and other properties between the NiAl and the Mo substrates;

- NiAl – Mo eutectics offer far higher fracture toughness than single phase NiAl;

- the NiAl – Mo eutectic is very shallow and so the operating temperature of the joint should be not much lower than that of the NiAl.

In any case, since the two substrate materials are effectively semi-infinite, prolonged holding at the bonding temperature would only increase the extent of eutectic melting of the substrates, rather than bringing about isothermal solidification. Thus, the in-situ bonding of NiAl – Mo remains a brazing (rather than a TLP bonding) process.

Results with the *in-situ* NiAl – Mo bonds were generally encouraging. However, the process needs to be carefully controlled for the following reasons: i) some superheat above the eutectic temperature is desirable for wettability, but if this is excessive then melting of the bulk NiAl will occur and ii) melting will take place readily as soon as the eutectic temperature is exceeded so only a very short bonding time is required.

III.4. Fracture Analysis

To employ the interferometry method for fracture analysis, it was necessary to fabricate joints of particular configurations. The joining task described above was unable to provide the sample needed for this analysis. The emphasis was therefore changed to develop the technique using a standard bimaterial configuration based on copper and aluminum.

III.4.a. Elasto-Plastic Interfacial Crack Tip Deformations using Infrared Interferometry

An infrared interferometer capable of performing real-time, full-field, non-contacting deformation field measurements on 'optically-rough' surfaces has been developed for elasto-plastic fracture mechanics investigations in bimaterial beams. The choice of the infrared wavelength allows high sensitivity interferometric measurements on fracture samples with little or no surface preparation and is more tolerant of the damage accumulation near the crack. The interferometer also bridges a sensitivity gap among existing techniques for out-of-plane displacement measurement. These features are essential for investigating failure of dissimilar material interfaces at elevated temperatures.

First, the range of surface roughness that can be studied using this interferometer is examined. Fringe contrast in excess of 0.5 can be realized with surfaces with roughness parameter $\hat{\sigma} = 0.8$ μm (or, $\hat{\sigma}/\lambda \cong 0.08$) while fringe contrast in excess of 0.8 can be obtained with roughness of $\hat{\sigma} = 0.35$ μm (or, $\hat{\sigma}/\lambda \cong 0.03$). In fact, the latter is shown to be easily achievable simply by polishing the sample surface with a #600 (mean grit size 15 μm) fixed abrasive. The proposed interferometer bridges the sensitivity gap between the visible light Twyman-Green interferometer (sub-micron sensitivity) and shadow/projection moiré methods (25-50 μm/fringe) used for mapping out-of-plane deformations.

Through AFoSR support, the feasibility of the sensor to investigate failure of bimaterial joints is carried out at room temperature. Interfacial crack tip deformations have been measured in elasto-plastically deformed solder-copper joints. The optical measurements are examined along with companion 2-D and 3-D elasto-plastic finite element simulations. Experimental measurement of elasto-plastic deformations near interfacial cracks are reported for solder-copper joints (figure 31). In the region $y > 0$ (solder half), 3-D deformations seem to dominate over $r/B \leq 0.5$ (r is the radial distance from the crack tip and B is the sample thickness) and along the interface. Due to the absence of explicit elasto-plastic interfacial crack tip solutions at the moment, the existence of a region of HRR-like deformation field is investigated and found to prevail over $0.5 \leq r/B \leq 0.75$ ahead of the crack (see figure 32).
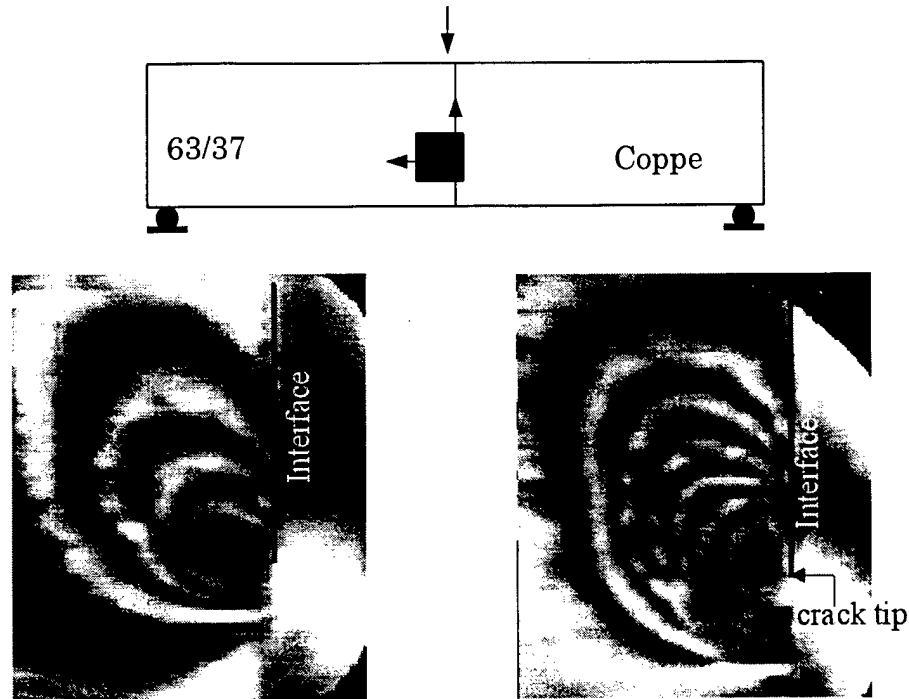
47

Figure 31. Fringe pattern near a soler-copper interface crack tip obtained using infrared interferometry. Note the severe asymmetry in the fringe patterns relative to the crack due to combination of elastic mismatch and intense plasticity effects.
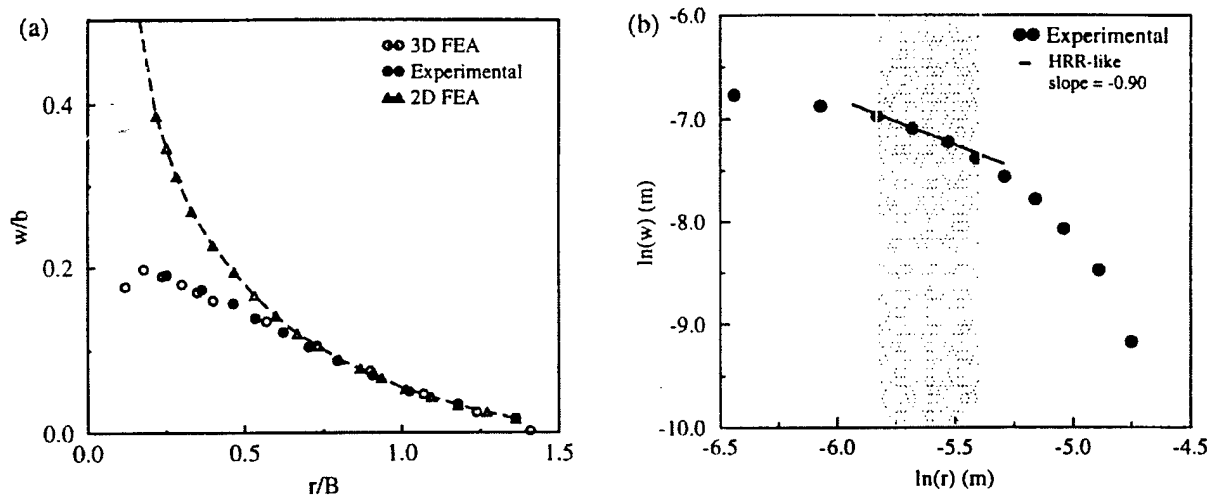

Figure 32. Crack tip three dimensionality and J-dominance in a solder-copper bimaterials beam: (a) plot of normalized displacements, (b) comparison of optical measurements with HRR prediction.

III.4.b. Strain Gage Method for Measuring Interfacial Fracture Parameters in Bimaterials

A technique for complex stress intensity factor (SIF) determination for bimaterial cracks using electrical strain gages has been developed. The asymptotic radial and hoop strain equations are used to compute SIF by linear transformation. The location of the strain gage relative to the crack tip is chosen through parametric study of asymptotic fields. The need for taking into account non-singular contributions to the crack tip strain field to accurately measure the magnitude and the phase of complex SIF is demonstrated. Low velocity impact experiments are conducted in bimaterial beams made by joining epoxy and glass-filled epoxy halves. During the experiments, these samples are loaded in three-point-bending configuration and the history of impact force and support reactions are measured and used as inputs in a dynamic finite element analysis. The simulations correspond to a dynamically loaded stationary crack tip. The computed and measured fracture parameters show good agreement until the time of crack initiation as shown in figure 33.
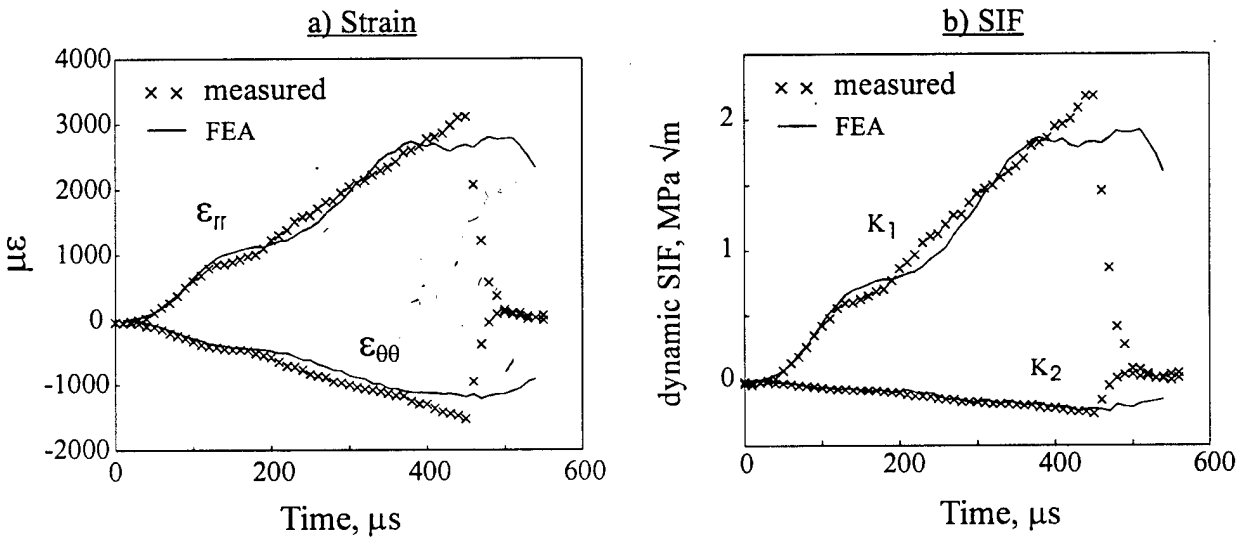

Figure 33. Comparison of measured strain and stress intensity factor results with FEA.

III.4.c. Bimaterial Joints with Similar Elastic and Dissimilar Plastic Characteristics

Fracture behavior of brittle dissimilar material interfaces using the notions of complex stress intensity factor and mode-mixity is widely studied in the literature. On the contrary, progress in understanding the plasticity effects on the interfacial fracture has been rather modest despite its practical significance in a wide range of dissimilar material systems. The work in this area has largely remained analytical/numerical in nature and experimental investigations are needed to further relate the local and global parameters and gain insight into the crack initiation and growth behaviors as in case of elastic counterparts. A detailed experimental study of the similarities (or the differences) of crack tip fields, mode-mixity, J-dominance, crack growth resistance, to name a few, would be valuable for modeling interfacial crack initiation and crack growth. To this end, an experimental effort on interfacial fracture behavior of bimaterials that are elastically similar but plastically dissimilar is considered. The research is aimed at gaining insight into the asymmetries introduced by plasticity parameters near the interfacial crack tip in bimaterial specimens that are dissimilar in their plastic characteristics but identical elastically.

Bimaterial samples were prepared by diffusion bonding different aluminum alloys with different heat treatments. Samples with (a) different yield stress but similar hardening exponent and (b) different hardening exponent but similar yield stress were prepared using the diffusion bonding method of transient liquid phase bonding. This allows delineation of the influence of individual material non-linearity parameters on interfacial fracture mechanics by studying elastically similar but plastically dissimilar bimaterials. Specifically, aluminum alloys namely Al 6061-T6 and Al 7075-T6 rolled stock was considered for the situation with different yield stress but nearly identical (low) hardening exponent. The combination of rolled and extruded stock of 6061 was used to realize the bimaterial combination with identical yield stresses but different hardening exponents. Bimaterial samples of this material combination were prepared using a 100 μm thick zinc foil as the interlayer material. The low melting point of zinc (420° C) allowed a rather low bonding temperature (500° C in this case). The bonding was performed in a Gleeble-1500 under vacuum conditions utilizing rapid thermo-mechanical cycling capability, servo-hydraulic loading system and direct resistance heating. The samples were characterized using light microscopy, scanning electron microscopy, x-ray spectroscopy and Vickers microhardness. High energy dispersive x-ray spectroscopy revealed that aluminum and zinc mainly concentrated near the bond line with zinc concentration decrease rapidly. Entry of zinc into the Al 6061 and Al 7075 substrates did not have discernable effect on the substrate microstructures. Meanwhile, zinc diffusion into the substrates did serve to reduce the average center-line zinc content to 4 at.%. Plots from the microhardness tests are shown in figures 34 and 35 showing sharp change in the values across the bond line in Al-6061/Al-7075 bimaterial and nearly flat response for the case of Al-6061 (rolled stock)/Al-6061 (extruded stock).
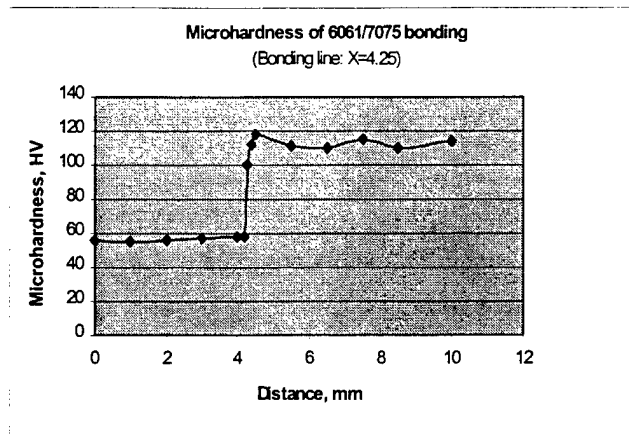
Figure 34. Microhardness profile of the joint between Al-6061 and Al-7075 showing abrupt change at the interface.
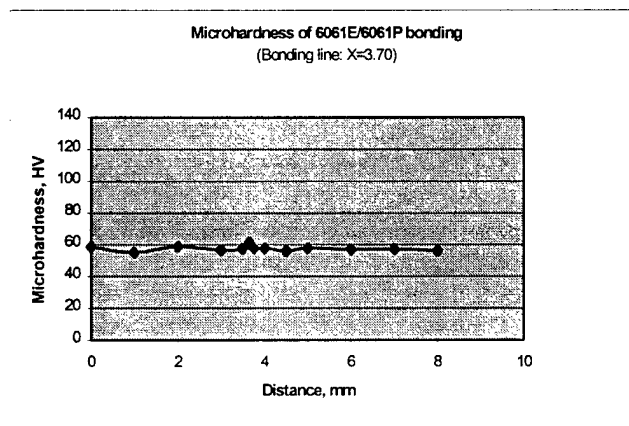

Figure 35. Microhardness profile of the joint between rolled and extruded Al-6061 showing a smooth transition.

IV. References

1. M.G. Houts, *27th Intersociety Energy Conversion Engineering Conference Proceedings*, San Diego, CA, Vol. 2 (1992) 245.

2. J. Liu, R.H. Zee and B.A. Chin, *J. Materials Processing Technology,* 89-90 (1999) 425.

3. H.S. Rhee, C. Zheng, J.K. Koester, A. Tastrebkov, Y. Nikolaev,and A. Gontar, *AIP Conference Proceedings 324*, Part One, ed. Mohammed S. EL-Genk, Albuquerque, NM, (1995) 389.

4. V.G. Glebovsky, V.N. Semenov and V.V. Lomeyko, *J. Crystal Growth,* 92 (1988) 8.

5. S. Otani, *J. Crystal Growth*, 51 (1981) 381.

6. S. Otani, *J. Crystal Growth*, 51 (1981) 431.

7. S. Otani, *J. Crystal Growth*, 83 (1987) 481.

8. S. Otani, *J. Crystal Growth*, 106 (1990) 489.

9. V.G. Glebovsky, V.N. Semenov and V.V. Lomeyko, *J. Crystal Growth,* 98 (1989) 487.

10. S. M. Copley and H. Kear, Trans. Metallic. Soc. AIME, 239, 977 (1967).

11. F. E. Heredia and D. P. Pope, Acta metall., 39, 2017 (1991).

12. K. Jumonji, T. Hinohara and M. Kato, Phil. Mag. Vol. 67, 627 (1993).

13. K. Aoki and Izumi, Tran. JIM, 19, 203 (1978).

14. K. Jumonji, S. Ueta, A. Miyahara, M. Kato and A. Sato, Phil. Mag. 73, 345 (1996).

15. Le Roy Roger Curwick, Ph.D. Dissertation, University of Minnesota (1977).

16. T. Hirano, Acta. Metall., 38, 2667 (1990).

17. C.W. Lan and S. Kou, J. Crystal Growth 118 (1992) 151.

18. H. Biloni, "Physical Metallurgy" ed. R.W. Cahn and P. Haasen, North-Holland Physical

Publishing, (1983) 511.

19. H. Biloni, "Physical Metallurgy" ed. R.W. Cahn and P. Haasen, North-Holland Physical Publishing, (1983) 498.

20. J. H. Bechtold, E. T. Wessel, and L. L. France, "Mechanical Behavior of the Refractory Metals", Refractory Metals and Alloys (edited by M. Semchyshen and J. J. Harwood), Detroit, Michigan, May 25-26, pp. 39, 1960.

21. R. T. Begley, D. L. Harrod and R. E. Gold, "High Temperature Creep and Fracture Behavior of the Refractory Metals", Proceedings of a Symposium on Metallurgy and Technology of Refractory Metals, Washington, D. C., April 25~26, pp.51, 1968.

22. H. W. King, "Quantitative Size-Factors for Metallic Solid Solutions", J. Mater. Sci., 1, 79-99 (1966).

23. R. E. Honig, "Vapor Pressure Curves of the Elements", Radio Corporation of America Laboratories, Sept 1962.

24. Y.S. Belomyttsev, S.N. Gundarev, L.V Demchenko, A.I. Dekhtytar, I.P. Zasorin, V.A. Kononenko, L.F. Matvienko, D.E. Ovsienko, and E.I. Sosina, *Izvestiya Akademmi Nauk SSSR. Metally 1* (1984) 90.

25. R.T. Begley, D.L. Harrod, and R.E. Gold, *Refractory Metal Alloys*, ed. I. Machlin, R.T. Begley and E.D. Weistert, Plenum, New York (1968) 41.

26. R.H. Erickse and G.J Janes, *Metallurgical Transactions 3* (1972) 1735.

27. H. Carvalhinhos and B.B. Argent, *Journal of the Institute of Metals, 95* (1967) 364.

28. W.D. Klopp, P.L. Raffo and W.R. Witzke, *Journal of Metals*, June (1971) 27.

29. H.S. Rhee, C. Zheng, J.K. Koester, A. Tastrebkov, Y. Nikolaev,and A. Gontar, *AIP Conference Proceedings 324*, Part One, ed. Mohammed S. EL-Genk, Albuquerque, NM, (1995)389.

30. N.G. Tachkova, P.V. Zubarev and A.A. Yastrebkov, *Izvestiya Akademii Nauk SSSR, Metally, 1*(1987) 153.

31. B.A. Wilcox, *Refractory Metal Alloys Metallurgy and Technology*, ed. I. Machlin, R.T.

Begley and E.D. Weistert, Plenum, New York (1968) 1.

32. H.P. Gao and R.H. Zee, *AIP Conference Proceedings 324, Part One, Albuquerque, NM,* (1995) 283.

33. H. Oikawa and T.G. Langdon, in *Creep Behavior of Crystalline Solids*, ed. B. Wilshire and R.W. Evans, Pineridge, Swansea (1985) 33.

34. T.G. Langdon, *Philosophical Magazine, 22* (1970) 689.

35. Binary Alloy Phase Diagrams, CD ROM edition, ASM International, Materials Park, OH, 1998.

36. H. Baker (Editor), Metals Handbook, Volume 3 (Alloy Phase Diagrams), ASM International, Materials Park, OH, 1992.

V. Papers and Presentations Resulting from Project Support

Publications

1. R.H. Zee, Z. Xiao, B.A. Chin and J. Liu, "Processing of Single Crystals for High Temperature Applications," accepted for publication in *Journal of Materials Processing*, November 2000.

2. M.K. Kitchings, W.F. Gale and Y. Guan, "Microstructural Development During Transient Liquid Phase Bonding of Structural Intermetallic Compounds," *Microstructural Sci.*, Accepted for Publication.

3. R.H. Zee, Z. Xiao, H.S. Gale, B.A. Chin and L.L. Begg, "Processing of Tungsten Single Crystals," accepted for publication in the *Proceedings of the Electrochemical Society*, May 2000.

4. T. Zhou, X. Wen, Y. Shen, Y. Xu and W.F. Gale, "Studies on the Diffusion Brazing of NiAl-Based Intermetallics", *Proceedings of International Brazing and Soldering Conference*, Submitted for Publication.

5. H.P. Gao and R.H. Zee, "Effects of Rhenium on Creep Resistance of Tungsten Alloys," submitted *to Journal of Materials Science Letters*, October 2000.

6. J. Liu, R.H. Zee and B.A. Chin, "Processing and High Temperature Properties of Refractory Alloy Single Crystals," *Journal of Materials Processing Technology* 89-90 (1999) pp. 425-431.

7. W.F. Gale, "Applying TLP Bonding to the Joining of Structural Intermetallic Compounds", *Journal of Metals*, **51 (2)**, 49 – 52, 1999 (Invited Paper).

8. P.R. Marur and H.V. Tippur, "A Strain Gage Method for Determination of Fracture Parameters in Bimaterial Systems," *Engineering Fracture Mechanics*, Vol. 64, No. 1, pp 87-104, 1999.

9. Z. Xiao and R.H. Zee, "Effects of Superheat and Growth Rate on the Crystal Growth Behavior of Ni_3Al," *Proceedings of the Third Pacific Rim International Conference on Advanced Materials and Processing*, Honolulu, Hawaii, edited by M.A. Imam, R. DeNale, S. Hanada, Z. Zhong and D.N. Lee, (TMS, Warrandale, PA) (1998) pp. 2:437-2:442.

10. J.K. Sinha and H.V. Tippur,, "An Infrared Interferometer for Elasto-Plastic Crack Tip Investigation of Homogeneous and Bimaterial Beams: A study of 3-D effects and J-dominance," ASME *Journal of Applied Mechanics*, Vol. 65, No. 4, pp 1032-1041, 1998.

11. J.K. Sinha and H.V. Tippur, "Elasto-Plastic Interfacial Crack Tip Field Investigation using Infrared Interferometry," Proceedings of the 1998 SEM Spring Conference, pp 331-335, Houston, TX.

12. W.F. Gale, Y. Guan and S.V. Orel, "Transient Liquid Phase Bonding of Structural Intermetallic Compounds," *J. Mater. Prod. Technol.*, 13, 1 – 12, 1998 (Invited Paper).

Presentations

1. W.F. Gale, "Studies on the Diffusion Brazing of NiAl-Based Intermetallics", Presented at the *International Brazing and Soldering Conference*, Albuquerque, NM, 2000.

2. Z. Xiao, R.H. Zee and L.L. Begg "Processing Tungsten Single Crystals," presented at the 2000 Space Technology and Applications International Forum, Albuquerque, NM February 2000.

3. J. Liu, R.H. Zee and B.A. Chin, "Processing and High Temperature Properties Of Refractory Alloy Single Crystals," presented at the Fourth Asia Pacific Conference on Materials Processing, Singapore, May 19-21, 1999.

4. R.H. Zee, "The Materials Issues for Power in Space," invited seminar in the Materials Science and Education Department in the City University of Hong Kong, May 17, 1999.

5. R.H. Zee, "The Materials Issues for Power in Space," presented as a seminar at the University of Alabama in Huntsville, May 5, 1999.

6. W.F. Gale, "Microstructural Development During Transient Liquid Phase Bonding of Structural Intermetallic Compounds", Presented at the *International Metallographic Society Convention*, Ottawa, Canada, 1998.

7. R.H. Zee, "Power and Propulsion in Space - The Materials Issue," presented as an invited seminar to the College of Engineering in the University of Hong Kong, September 11, 1998.

8. P.R. Marur and H.V. Tippur, "A Strain Gage Method for Determination of Fracture

Parameters in Bimaterial Systems," presented at ASME IMECHE, Dallas, TX, November 1998.

9.   Z. Xiao and R.H. Zee, "Effects of Superheat and Growth Rate on the Crystal Growth Behavior of Ni_3Al," presented at the Alabama Materials Research Meeting, Birmingham, AL, September 1998.

10.   Z. Xiao and R.H. Zee, "Effects of Superheat and Growth Rate on the Crystal Growth Behavior of Ni_3Al," presented at the Third Pacific Rim International Conference on Advanced Materials and Processing, Honolulu, Hawaii, July 12-16, 1998.

11.   Z. Xiao and R.H. Zee, "Ductility of Ni_3Al Single Crystals at Elevated Temperature - Effects of Preoxidation," presented at the 127 Annual TMS Meeting, February 15-19, 1998.